Article:
Okenyi, V., Afazov, S., Mansfield, N. et al. (2025) Submerged arc welding of S355G10+M steel: analyzing strength, distortion, residual stresses, and fatigue for offshore wind applications. Fatigue & Fracture of Engineering Materials & Structures, 48 (9). pp. 3859-3878. ISSN: 8756-758X

https://doi.org/10.1111/ffe.70010

Fatigue & Fracture of Engineering Materials & Structures

WILEY

FFEMS Fatigue & Fracture of Engineering Materials & Structures

ORIGINAL ARTICLE OPEN ACCESS

Submerged Arc Welding of S355G10+M Steel: Analyzing Strength, Distortion, Residual Stresses, and Fatigue for Offshore Wind Applications

Victor Okenyi[1] | Shukri Afazov[1] | Neil Mansfield[1] | Jeyaganesh Balakrishnan[2] | William Kyffin[2] | Petros Siegkas[3] | Tiziana Marrocco[4] | Mahdi Bodaghi[1]

[1]Department of Engineering, School of Science and Technology, Nottingham Trent University, Nottingham, UK | [2]Nuclear Advance Manufacturing Research Centre, University of Sheffield, Rotherham, UK | [3]Department of Mechanical Engineering and Materials Science and Engineering, Cyprus University of Technology, Limassol, Cyprus | [4]Advanced Materials Research Laboratory, University of Strathclyde, Glasgow, UK

Correspondence: Victor Okenyi (victor.okenyi@ntu.ac.uk)

Received: 25 January 2025 | **Revised:** 19 May 2025 | **Accepted:** 7 June 2025

Keywords: fatigue | mechanics of materials | residual stresses | S355G10 +M structural steel | submerged arc welding | thickness effect

ABSTRACT

This research delves into the material performance of submerged arc-welded S355G10 +M structural steel for offshore wind turbines, with an emphasis on strength, ductility, hardness, distortion, residual stress, and fatigue. This was done by conducting experiments and employing modeling tools combined with image analysis. The novelty of this study lies in examining the effects of material properties of S355G10 +M structural steel used in welded offshore wind turbine tower and monopile. The study employed a submerged arc welding (SAW) process on S355G10 +M plates of varying thicknesses by applying double V-groove and multi-pass technique. Tensile tests revealed that welded sections exhibit greater ultimate tensile strength than the base material, despite the lower yield strength. In addition, hardness and residual stresses correlate with thickness, and a potential weak point is observed at the heat-affected zone (HAZ) and base material transition. Angular distortions and axial misalignments after welding, as well as stress concentrations and residual stresses, were found to affect the fatigue performance. It was concluded that the conducted welds have sufficient quality to be exploited into industrial marine applications including offshore wind turbines.

1 | Introduction

As the need for installing offshore structures grows, it becomes important to understand and improve their material performance at design and fabrication stages. These are part of measures to solve current installation and in-service challenges, such as reducing manufacturing costs, mitigation of corrosion, fatigue, and even collapse. Thus, understanding the mechanical properties, welding processes, and resulting phenomena such as distortion and residual stresses is critical to understanding the performance of mild-to-medium strength range structural steels. S355 structural steel, widely used in offshore, shipbuilding, and construction industries, is known for its excellent weldability and durability [1], as well as for its corrosion and fatigue characteristics. This grade of structural steel has shown promising performance as it is often used in critical joints in support structures of offshore wind turbines (OWT) [2–4]. To optimize the manufacture and use of S355 structural steel applied in the fabrication of large-diameter OWT monopiles, tensile, and hardness testing, analysis of arc welding processes used in their manufacturing and their impact on distortion and residual stress are necessary.

Abbreviations: AW, As-welded; BM, Base metal; CAD, Compute aided design; CMM, Coordinate measuring machine; DPI, Dye penetration inspection; FEA, Finite element analysis; HAZ, Heat affected zone; OWT, Offshore wind turbines; SAW, Submerged arc welding; SCF, Stress concentration factor; S–N, Stress–number of cycles; UTS, Ultimate tensile strength; WEDM, Wire electro-discharge machining.; WM, Weld material.

Summary

- This research examines submerged arc-welded S355G10 +M properties for offshore applications.
- This study assesses thickness effects on submerged arc-welded S355G10 +M steel.
- Welded S355G10 +M shows higher ultimate strength than base material.
- Fatigue is driven by residual stresses, stress concentration, and distortions.

Tensile tests are crucial for determining the strength and ductility of welded S355 structural steel, as they provide information on the material's ability to withstand applied loads without reaching the elastic limit/yield stress of the material. These tests are typically performed according to standardized procedures such as the ASTM E8 to ensure reliable and reproducible results [5]. When structural steel is welded, the characteristics of the weld and the heat-affected zone (HAZ) change significantly. In addition to the tensile tests, hardness tests are a simple way to find out how resistant a material is to deformation or wear [6].

Submerged arc welding (SAW) is a technology used to join mild-to-medium strength range structural steels. It has benefits such as high deposition rates, good weld quality, and the ability to be automated. The process employs a continuous, consumable electrode and flux layer that submerges the molten weld pool, protecting it from atmospheric contamination and minimizing defects that could compromise the mechanical properties of the welded joint. Despite its many advantages, SAW can introduce distortion and residual stress in welded S355 structural steels, which can negatively impact their performance [7, 8]. The introduced distortion and residual stresses during SAW can lead to reduced service life [9–16]. Therefore, it is crucial to understand the formation of distortion and residual stress from the SAW process and how they can affect the performance of S355 structural steels.

Residual stresses are generated due to the nonuniform temperature distribution during the welding process and the associated thermal strains, which can cause the material to yield locally and have great influence on fatigue crack initiation and growth [17, 18]. Upon cooling, the welded joint contracts, resulting in tensile residual stresses that can negatively impact the component's fatigue life, fracture toughness, and increase susceptibility to stress corrosion cracking [19]. The effect of postweld treatment procedures has been observed to mitigate residual stress effects and enhance the fatigue life of multipass-welded S355 structural steel used in OWT monopile weldment as well as shot-peening by creating compressive in-plane residual stresses that can enhance fatigue performance [20].

Welding-induced distortion is caused by the impact of the residual stresses [21, 22]. Factors influencing distortion include welding sequence, fixture positioning, and welding parameters (e.g., current, voltage, and travel speed) [23–26]. When a welded structure is distorted, it loses its dimensional precision, which can impact the stress distribution after a load is applied.

Research on distortion prediction models for arc-welded structural steels and their mitigation has been extensively conducted on various butt-welded materials using experimental and numerical methods [25, 27–30], which provide a basis for evaluating expected distortion levels and validating predictive models used in this study. In addition, machine learning methods have also been implemented to reduce weld defects and improve process control, as demonstrated in studies using artificial neural networks and deep learning for real-time monitoring [31, 32]. Residual stress studies have been researched in different welded structural steels, which inform the selection of techniques used in this work to characterize residual stress in thick-section S355G10 +M welds [21, 33–36]. Also, the residual stress impact on the fatigue life has been investigated [7, 17, 18, 37–39] demonstrating how residual stress and microstructural changes influence fatigue crack initiation and growth factors, as investigated in our fatigue characterization of S355G10 +M. These residual stress studies discussed that residual stresses change significantly in welded structures with complicated shapes. This makes it more difficult to predict the fatigue performance of butt-welded S355 steel structures of actual size from lab-scale specimens. In contrast to the previously conducted research, this study primarily focuses on the S355G10 +M structural steel used for OWT towers and monopiles, as well as other marine structures. The processing of S355G10 +M structural steel with SAW is a viable option for the installation of OWTs. Therefore, fundamental research on understanding the mechanical performance of welded S355G10 +M samples with SAW is vital and beneficial for the OWT industry.

To further highlight the importance of fatigue and corrosion in these structures, relevant literature is discussed below. Fatigue in OWT support structures arises from cyclic marine loading, with corrosion significantly accelerating fatigue damage. Suresh [40] defined corrosion-fatigue as damage from cyclic stresses in corrosive environments, emphasizing its relevance for marine structures. Dong et al. [41] highlighted how pitting corrosion accelerates crack propagation, making it a dominant failure mode. Given that 98% of offshore foundations rely on structural steel [42], understanding corrosion-fatigue mechanisms is vital. Melchers [43] provided further insight into pit development and its role in long-term structural degradation.

Corrosion-fatigue has been studied across several industries including marine, aerospace, and construction due to its impact on lifespan and failure rates [44]. Price and Figueira with Okenyi et al. [4, 44] identified uniform, pitting, and corrosion-fatigue as the primary degradation modes in OWT foundations. Monitoring these effects is particularly crucial in the splash zone. Monopiles are the dominant foundation type for OWTs due to their simplicity and scalability [45], yet their fatigue behavior requires further study. The role of welding quality and residual stresses is significant, especially in the HAZ, affecting fatigue resistance [3, 46, 47]. Hence, a robust assessment of mechanical and fatigue properties in welded S355G10 +M steel is both timely and necessary.

This research aims to explore the material performance of submerged arc butt-welded S355G10 +M structural steel for high-capacity OWT applications. While previous studies have addressed fatigue, corrosion, and weld-induced stresses in structural steels, few have offered a comprehensive evaluation focused on this thermo-mechanically rolled steel increasingly used in thick-section offshore monopiles and other offshore structures. Also, most existing studies focus narrowly on fatigue crack growth rate, ignoring the role of residual stress and weld-induced distortion This study addresses key gaps in the current literature on S355G10 +M by investigating fatigue performance as influenced by the combined effects of mechanical properties, metallurgical changes, and geometric factors to provide a holistic understanding of weld implications that can affect material performance. Therefore, the novelty of this work lies in its integrative investigation of mechanical performance, including tensile strength, ductility, hardness distribution, angular distortion, residual stress, and fatigue behavior across multiple thicknesses, using SAW with a double V-groove multipass technique.

2 | Manufacturing of Specimens

2.1 | SAW Process Producing Butt-Welded Plates

As-welded (AW) S355G10 +M plates of four different thicknesses (6, 10,15, 20 mm) have been produced using single-wire SAW. The selection of these thicknesses represents the lower range of thicknesses used for OWT tower and monopile thickness varying from 6 mm to 100 mm [48, 49]. In addition to OWT towers and monopiles, the investigated thickness could find useful applications in other marine industries (i.e., ships and submarines) for design optimization and ensuring structural integrity. The dimensions of the plates for the four thicknesses had a surface area of 1000 mm × 200 mm after welding.

The S355G10 +M has been used for the manufacture of OWT monopiles [2, 50]. Table 1 contains information on the chemical composition of the base metal (BM) and the weld material (WM) which had a solid wire electrode to be EN ISO 14171-A: S3Si (IABCO 2.4/3.2 mm), and the flux was EN ISO 14174: SA FB 155 AC H5. The mechanical properties of the base structural steel material are also presented in Table 1 according to the manufacturer's specifications, and the WM tensile properties were higher than those of the BM, as presented. Mechanized high-quality SAW was conducted on hot-rolled plates by the Nuclear Advanced Manufacturing Research Centre to industry standards and specifications.

Double V-grooves were machined at the edges for better welding as illustrated in Figure 1a. The machined steel plate edges were cleaned with acetone to remove dirt and any other oil contaminants. The plates were aligned and clamped in place with a fixture to ensure a good fit with minimal gaps. This was followed by setting up the SAW equipment comprising a power source, wire feeder, welding torch, and flux delivery system. The solid wire electrode and flux were selected with S355 G10 +M steel for a strong weld. The welding settings that were used (wire feed speed, voltage, travel speed based on the material's thickness, and joint design) are presented in Table 2. The joint was supplied flux through a flux hopper to protect the molten weld pool from air. An arc formed between the flux-submerged steel plates and the electrode. Heat from the arc melted the electrode, flux, and base material. This created a steady-speed molten weld pool along the joint. The multipass welding sequence conducted for each thickness is illustrated in Figure 1b. There were more passes for the thicker plates. The dwell time, which is the period allowed for the welded area to cool before another layer of weld is applied for successive layers, was approximately 12 min with interpass temperature ranging between (21°C–133°C) across specimen thicknesses. After each weld pass, the weld bead

TABLE 1 | Chemical and mechanical composition of S355G10 +M.

Chemical properties									
Base metal—Element (wt%)									
C	Si	Mn	P	S	N	Al	Cu	Cr	Ni
0.07	0.25	1.37	0.014	0.003	0.005	0.048	0.03	0.04	0.04
V	Ti	Nb	Mo	B	EV3[a]	EV4[b]	Nb + V		
0.004	0.014	0.03	0.001	0.0003	0.11	0.05	0.03		
Weld metal—Element (wt%)									
C	Si	Mn	P	S	Cr	Ni	Mo	Cu	N
0.11	0.3	1.75	0.007	0.005	0.03	0.02	< 0.01	0.01	0.004

Mechanical properties from manufacturer			
Material	**Yield stress (MPa)**	**Ultimate tensile strength (MPa)**	**Elongation (%)**
Base metal	422–510	483–559	27–30.5
Weld material (AW)	501	590	29

[a]EV3 = V + Nb + Ti.
[b]EV4 = Cr + Cu +Mo + Ni.

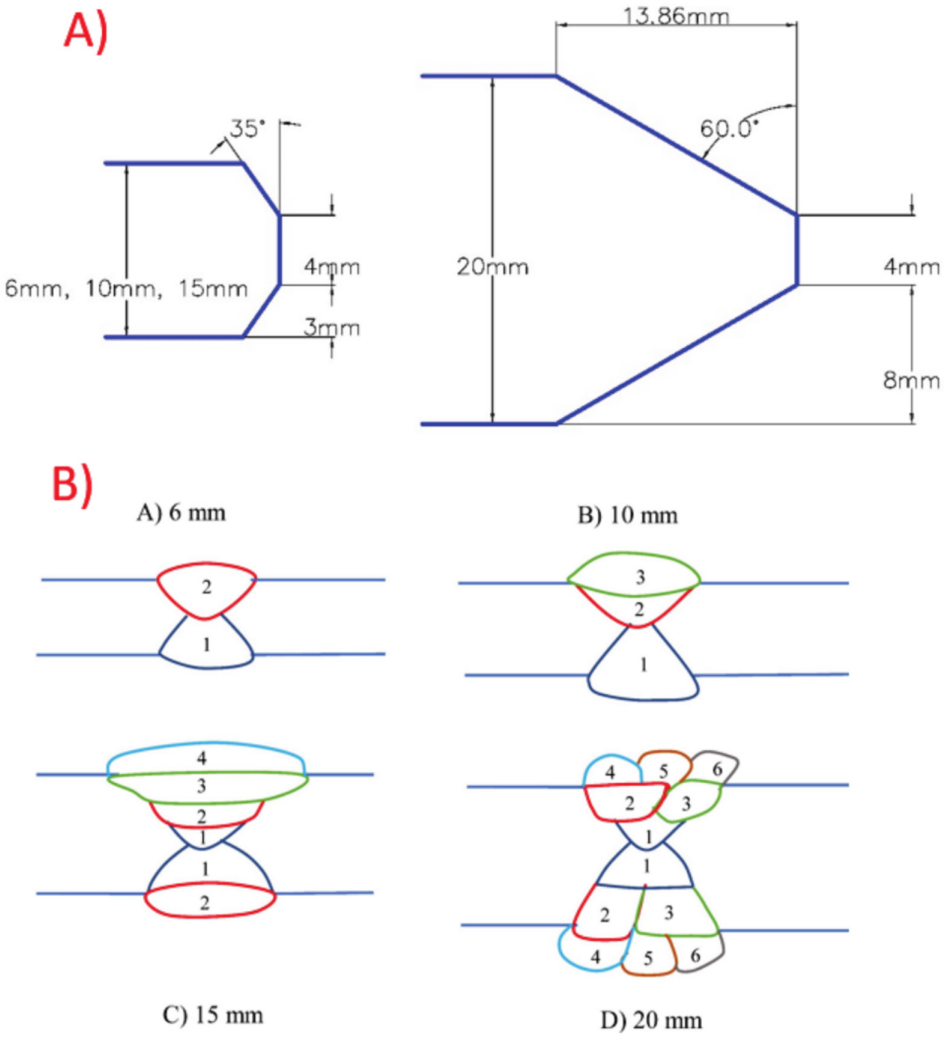

FIGURE 1 | Butt welding preparation showing (A) edge preparation and (B) deposition sequence. [Colour figure can be viewed at wileyonlinelibrary.com]

TABLE 2 | Welding process parameters for butt-welded S355G10 +M structural steel.

	Values based on thickness			
Parameters	**6 mm**	**10 mm**	**15 mm**	**20 mm**
Current (A)	390	393.3	396.6	400
Arc voltage (V)	26.5	27.6	27.8	28
Wire feed rate (m/min)	1.7	1.7	1.7	1.7
Wire stick-out (mm)	25	25	25	25
Travel speed (mm/min)	390	383.3	363.3	383.1
Preheat/interpass (°C)	21–36	21–70	21–90	21–133
Heat input (kJ/mm)	1.6	1.7	1.8	1.7
Current polarity	DC+	DC+	DC+	DC+

cooled and hardened, and the flux turned into a solid slag layer that was removed with a wire brush. After welding, to check the weld beads for its surface quality, visual inspection, and dye penetration inspection (DPI) were conducted as a nondestructive testing method according to BS EN ISO 23277 [51]. This was done to ensure that joint flaws or cracks are not present. The illustration of the SAW processes is summarized in Figure 2. No postweld heat treatment was applied as part of understanding the material properties. Table 3 highlights the plate and specimen designations used in this study for measurement and experiment tracking. It is imperative to highlight that welding practices were designed and executed in compliance with the BS EN 1011 standard for arc welding of steels [52]. Prior to the commencement of the main welding process, preliminary trials were conducted to optimize the welding parameters and weld quality. These trials included the current and voltage settings to ensure best weld metal penetration, welding speed to ensure uniform weld bead, and interpass temperature to ensure optimal cooling rate which in turn affects the mechanical property of the welded S355 G10 +M steel. We performed Design of Experiments trials with each welding parameter (e.g., current, voltage, and travel

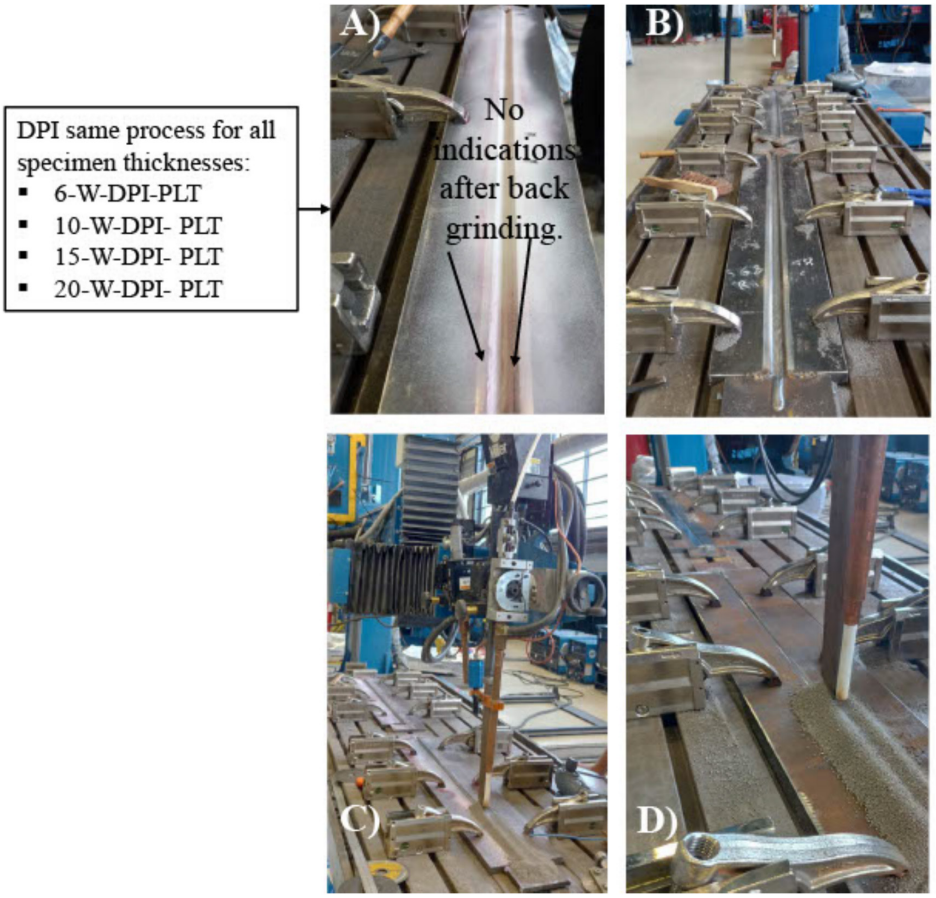

FIGURE 2 | SAW process stages: (A) After DPI. (B) Plate clamping. (C) Welding setup. (D) SAW process for all specimens. [Colour figure can be viewed at wileyonlinelibrary.com]

TABLE 3 | Specimens designation and experiments tests.

		Thicknesses and designation (P—plain specimens, W—welded specimens, PLT—plates)			
Experiments	**Notation**	**6 mm**	**10 mm**	**15 mm**	**20 mm**
Dye penetration inspection	DPI	6-W-DPI-PLT	10-W-DPI-PLT	15-W-DPI-PLT	20-W-DPI-PLT
Tensile tests	TT	6-P-TT, 6-W-TT	10-P-TT, 10-W-TT	15-P-TT, 15-W-TT	20-P-TT, 20-W-TT
Macrostructure	M	6-W-M	10-W-M	15-W-M	20-W-M
Hardness	H	6-W-H	10-W-H	15-W-H	20-W-H
Bending distortion	BD	6-W-BD-PLT	10-W-BD-PLT	15-W-BD-PLT	20-W-BD-PLT
Angular distortion	AD	6-W-AD-PLT	10-W-AD-PLT	15-W-AD-PLT	20-W-AD-PLT
Axial misalignment	AM	6-W-AM-PLT	10-W-AM-PLT	15-W-AM-PLT	20-W-AM-PLT
Residual stress across weld	RAC	6-W-RAC	10-W-RAC	15-W-RAC	20-W-RAC
Residual stress along weld	RAL	6-W-RAL	10-W-RAL	15-W-RACL	20-W-RAL
Fatigue test	F	6-W-F	10-W-F	15-W-F	20-W-F

speed) being varied individually while all other parameters are kept constant for thicknesses of 6–20 mm. Parameters such as current (390–400A), arc voltage (26.5–28 V), travel speed (363.3–390 mm/min), interpass temperature (21°C–133°C), and heat input (1.6–1.8 kJ/mm) were varied, as shown in Table 2. These adjustments ensured optimal penetration, uniform bead appearance, and controlled cooling rates, enhancing weld quality and integrity.

2.2 | Water Jet Cutting and Wire Electro-Discharge Machining of Butt-Welded Plates

In the preparation of specimens for testing, waterjet cutting was performed on four welded plates, each of which had a different thickness. The cutting was conducted on plates 330mm × 200 mm which were cut from the SAW plates with dimensions 1000mm × 200 mm. Waterjet cutting was performed in a high-precision process using an 87,000 Psi Dynamic Waterjet XD machine. This technology uses a high-pressure jet of water mixed with a garnet abrasive, providing a cold-cutting process that avoids issues in the HAZ, stress generation, and structural changes seen in traditional methods like cropping, laser cutting, or plasma cutting. Figure 3 shows the specimen faces after WEDM with a reference made to specimens along the weld and across the weld. Distortion and misalignments are measured and discussed subsequently to analyze the material and how this affects fatigue. The Sodick AQ750L WEDM system was employed with a wire diameter of 0.25 mm. To prevent breakage of the wire, the feed rate was controlled using a variable circuit for the different sections of the plates. The average speed of the wire was recorded to be 1.4 mm/min for all plates. Practically, producing welded samples with zero angular distortion is unlikely, the samples with the least distortion were selected for the study. The distance between the cutting surface and the toe should has been kept within 1–2 mm from weld toe.

3 | Tensile Testing Results

Across-weld specimens were tested to understand the tensile properties of the material. The purpose of the static tensile testing was to extract the mechanical properties and compare the yield strength as well as the ultimate tensile strength reported by the material supplier. Static tensile testing was conducted in accordance with the ASTM E8 standard [5] using standardized specimen geometries prepared from different thicknesses of welded structural steel. Figure 4 displays the specimen's dimensions, and the testing equipment used was a 400-kN uniaxial servo-hydraulic system. The equipment was checked for accuracy and calibrated before the test sequences began. The accuracy of the load cell and measurements of displacement under both no-load and loaded situations were checked to make sure the system was accurate following the ASTM E8 standard [5]. The stress–strain relationship was obtained up to the point of failure. To verify the supplier's values, welded and plain specimens of each thickness were evaluated. The loading rate was 2 mm/min.

Figure 5 shows fractured specimens in the base material close to the edge of the HAZ, indicating that the welded section was constructed from a stronger WM, as supported by the yield and the ultimate tensile stress values in Table 1. Moreover, as reported

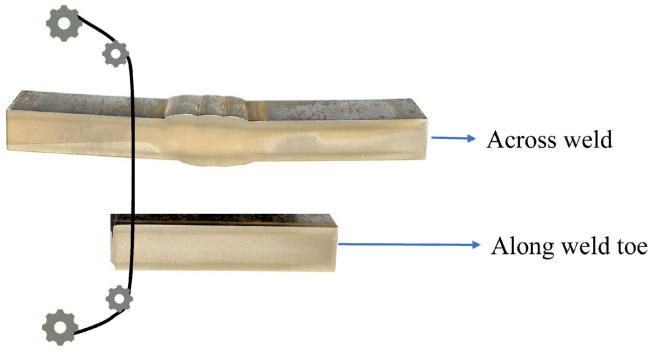

FIGURE 3 | Specimens showing the cut directions after wire electro-discharge machining. [Colour figure can be viewed at wileyonlinelibrary.com]

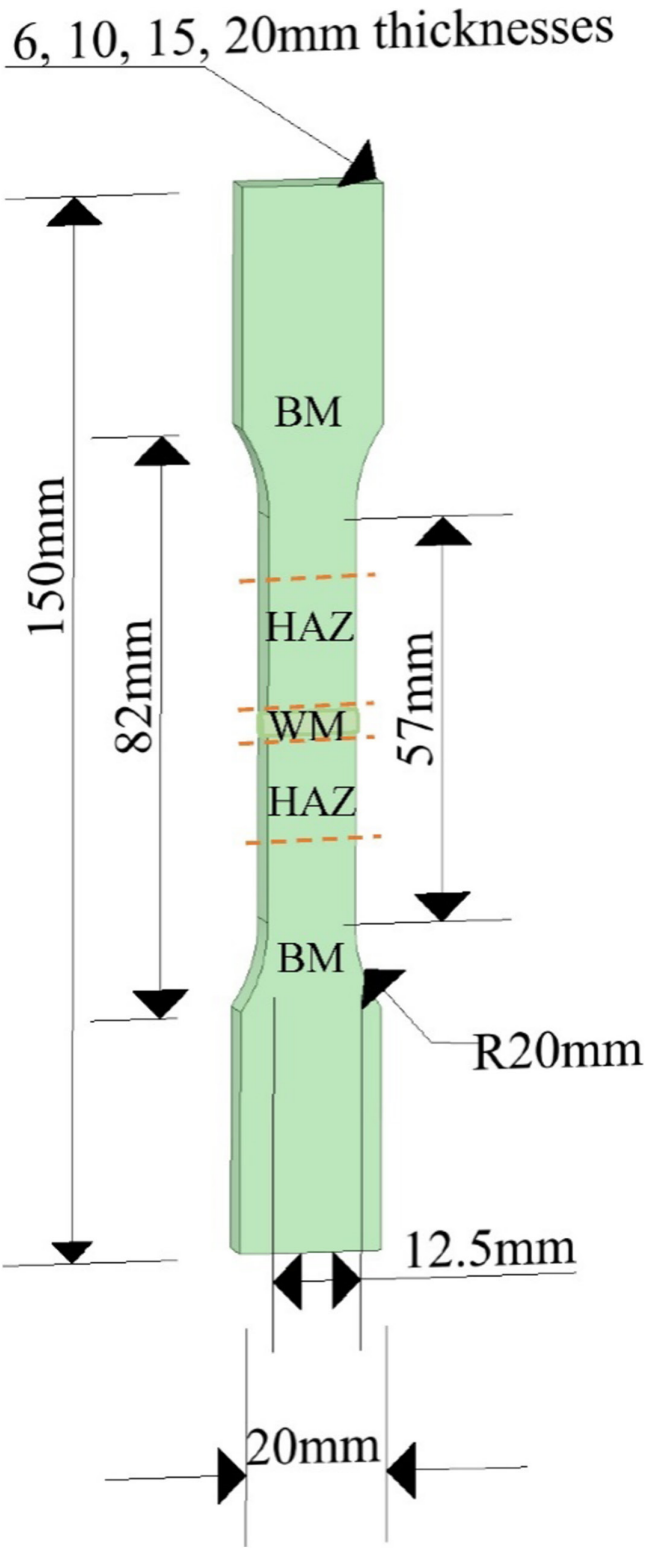

FIGURE 4 | Tensile tests specimen dimensions. [Colour figure can be viewed at wileyonlinelibrary.com]

from static tensile testing of other S355 material variations, specimens also fractured in the BM [7, 12]. The extracted mechanical properties from the stress–strain relationships for all plain and welded specimens are presented in Table 4, while Figure 6 shows an example of stress–strain data for specimens with a thickness of 6 mm. Due to the high loading forces and limited grip area of the samples during the tensile testing, minor oscillations in the hardening zone were observed in several of the recorded stress–strain curves. These fluctuations were caused by slight instabilities at the grips and did not significantly affect the determination of key mechanical properties. This can suggest that larger grip area is advisable for thicker specimens than 20 mm. The 0.2% offset approach was used to obtain the yield stress, which ranged from 361.4 MPa to 438.9 MPa. Stress–strain relationships for all plain and welded specimens are presented in Table 4. The obtained strengths were either close to or slightly lower than those listed by the supplier. Nonetheless, the mechanical properties were above the desired strength levels, indicating the quality of the weld. The value of the yield strength from testing in the plain specimens decreased with an increase in plate thickness as reported elsewhere [1, 2]. The same observation was made for the welded specimens in this study too. The yield strength was lower for the welded specimens, but they had higher ultimate strength, causing the failure at the BM. The ductility, measured as the amount of plastic deformation that occurs before fracture, was greater in the plain specimens than in the welded specimens. In addition, the elongation before fracture in the welded specimens was lower than that in the plain specimen, indicating that the welded specimens were more brittle.

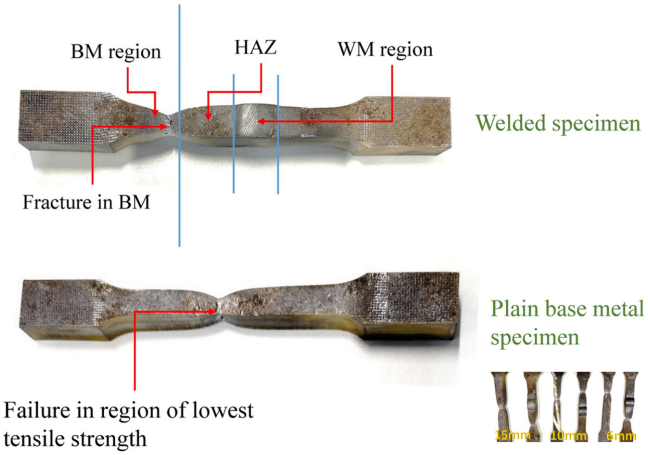

FIGURE 5 | Tensile failure in specimen typical for all thicknesses. [Colour figure can be viewed at wileyonlinelibrary.com]

There are differences observed in conducting static tensile tests on plain BM and welded specimens as shown in Figure 5. Failure occurred in the region of the plain specimen that had the lowest tensile strength, whereas for the welded specimen, tensile failure occurred in the BM owing to the strong weld quality and the fact that the localized increase in stress exceeded the strength of the adjacent BM, leading to failure in the BM region. It is important to note that the specimen geometry includes a reduced section with a fillet radius, which may act as a stress concentrator. However, failure consistently

TABLE 4 | Tensile test results for butt-welded S355G10 +M steel.

Specimen	Cross sectional area (width × thickness)	Yield stress (MPa)	Ultimate tensile stress (MPa)	Elongation (%)
6-mm specimens (manufacturer specification)	124.6	455	515	30.2
6-P-TT	75.6	447.3	493.7	22.7
6-W-TT	76.3	436	505.1	19.7
10-mm specimens (manufacturer specification)	200.0	510.5	559	28.5
10-P-TT	124.0	438.9	515.4	25.4
10-W-TT	125.0	432.6	552.6	16.6
15-mm specimens (manufacturer specification)	300.0	422	483	30.5
15-P-TT	186.3	363	469.6	27.3
15-W-TT	186.5	338.6	519.4	20.1
20-mm specimens (manufacturer specification)	400.0	467.8	535	27
20-P-TT	252.0	362.8	520.9	26.5
20-W-TT	255.3	361.4	524.8	20.3

occurred away from the weld and HAZ, supporting the observation that the weld was not the weakest region under the applied loading. There is a more uniform stress distribution in the plain specimens over their cross section, whereas in welded specimens, stress distribution is affected by residual stresses and microstructural variations from welding. The plain specimens provided the S355G10 +M inherent properties, while the welded specimens provided an understanding of the joint properties. Also, since both plain and welded specimens fail in the BM, it suggests that the BM is the weakest part of the sample under the given conditions, and the strength of the BM in the vicinity of the weld may have been altered due to the thermal cycles during welding.

4 | Weld Macrograph and Hardness Test Results

Several variables can affect the structure of the S355G10 +M including the chemical composition, thermal treatment, and cooling rates. Controlled rolling and cooling enhance the microstructure of thermo-mechanically controlled steel, achieving an optimal balance of strength, ductility, and toughness for engineering applications.

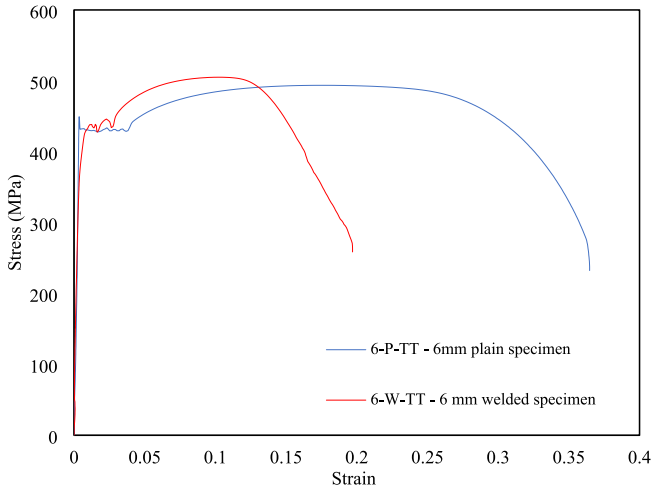

FIGURE 6 | An example of a stress–strain relationship for plain and welded specimens. [Colour figure can be viewed at wileyonlinelibrary.com]

Welded specimens were subjected to cross-sectional processing for macroscopic observation. They were sanded using silicon carbide sheets of grades 60, 120, 240, 320, 400, 600, and 800, then etched with 12 M of solution of hydrochloric acid. The HAZ was the primary focus of the macrographs since fatigue tests have indicated that it is a probable failure point [3, 53, 54]. The Brinell hardness was determined by measuring cross-sections taken from different parts of the material to compare the hardness levels in the BM, HAZ, and WM areas. The hardness measurements were done using 100-kN universal testing equipment in line with EN ISO 6506-1 [55]. It was ensured that the surfaces of selected specimens were free of imperfections and smooth from polishing to ensure proper indentation. A force of 20 kN was applied across the steel cross-section and held for 15 s from the 10-mm diameter indenter. Up to two specimens were used for each thickness to capture more data across all the regions of the specimen. The diameter of the spherical indentation was then measured using a macroscopic scale from which hardness values were obtained, and subsequently, contour plots were obtained based on the coordinates using MATLAB [56].

4.1 | Macrostructure Inspection

Figure 7 shows the morphologies of the grains in the WM and HAZ. During the SAW process that was carried out on the S355G10 +M plates, the morphology of the grain can serve as an indicator of the quality and integrity of the weld. The columnar grains in the WM are typical for the welding process due to the phase from liquidus to solidification state of the material. The grains in the HAZ were equiaxed and smaller in size. Other than etching pores, the outstanding quality of the weld is demonstrated by the absence of any readily apparent flaws, such as porosity, hot cracking, or keyholes.

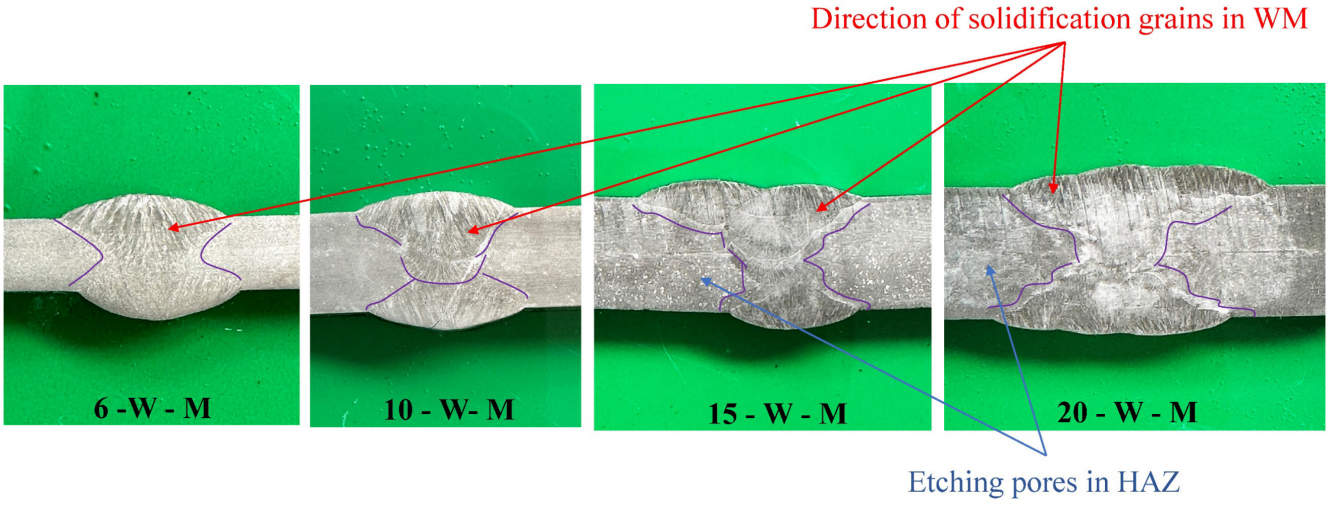

FIGURE 7 | Cross-section of macrostructure highlighting weld passes and grain morphology. [Colour figure can be viewed at wileyonlinelibrary.com]

The microstructural features of S355G10 +M structural steel play a pivotal role in defining its mechanical performance, particularly in demanding offshore and marine environments [57]. These environments necessitate a balance in the microstructure to enable the steel to withstand harsh conditions, such as corrosive environments, dynamic loads, and high pressure, which are characteristic of offshore applications.

The grain size and composition in Figure 7 are keys to structural integrity. The fine-grained structure, especially in the weld metal (WM), enhances yield and tensile strength, providing necessary strength and hardness to resist impact and static loads in offshore environments [46, 58]. The presence of manganese, nickel, and chromium from Table 1 enriches the structure with enhanced corrosion resistance, strength, and toughness [59]. Corrosion resistance is of high importance in marine environments for maintaining the structural integrity of offshore structures [60–62]. The control and optimization of microstructural elements in S355G10 +M are vital for the mechanical performance needed in offshore and marine applications.

4.2 | Brinell Hardness Results

The results of the hardness tests are plotted and reported in Figure 8 for specimens ranging in hardness from 6-mm welded specimens to 20-mm welded specimens. Meyer's law relates the Brinell hardness to ultimate tensile strength by using a constant that is material dependent [63]. However, according to Table A1, ISO 18265:2003 [64], which establishes a more material specific relationship between hardness values and tensile strength of metallic materials for the S355 structural steel considered in this study, the BM, HAZ, and WM for 6, 10, 15, and 20 mm have average values of 125, 137.5, 150, and 175 HB, respectively. This corresponds to tensile strength values of 415, 465, 509, and 594 MPa, which when compared to Table 4, it can be seen a reasonable tensile strength prediction.

Figure 8 illustrates that the hardness values increased as the specimen thickness increased, with the greatest value at 207 HB occurring in the WM for the 20-mm welded specimens. The values for the hardness reduced by moving from the HAZ to the BM. This hardness value is consistent with the values reported in the literature for other S355 alloys [65–68]. This suggests that high values of hardness are to be anticipated in the monopiles of OWT that range in thickness from 65 to 90 mm. In addition, it was observed that as the thickness of the specimens increased, the width of the HAZ increased too. This can be explained by the fact that a rise in thickness necessitates the execution of more weld passes, requiring more heat energy input, which in turn leads to an expansion in the width of the HAZ. Figure 11a–d showed that a region is shared by both the HAZ and the BM. This region had a low value of hardness, and it was found that this was also the region where the materials failed in the static tensile tests (see Figure 5). This shows that hardness measurements can indicate the failure point for static tensile testing by identifying the weakest region. This can be explained by a change in the microstructure of the material in the transitioning zone.

The observed increase in hardness with specimen thickness in thicker monopile sections suggests improved deformation

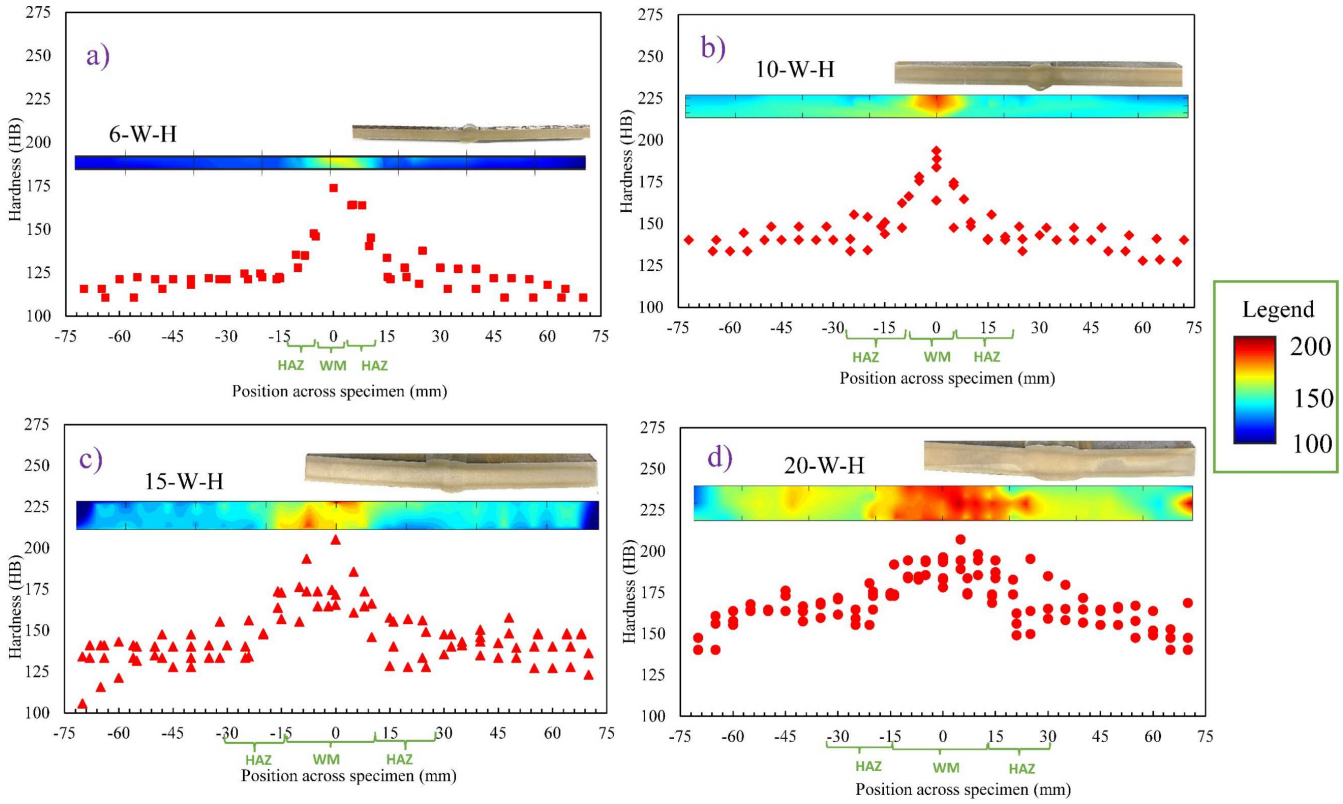

FIGURE 8 | Hardness results (HB) for (a) 6-mm, (b) 10-mm, (c) 15-mm, and (d) 20-mm welded specimens. [Colour figure can be viewed at wileyonlinelibrary.com]

resistance, potentially enhancing performance under high-stress conditions typical OWT applications. However, excessively high hardness could reduce ductility, increasing brittleness, and the risk of brittle fracture. Additionally, the observed decrease in hardness in the transition zone between the HAZ and BM raises concerns, as regions with reduced hardness may compromise structural integrity. Microstructural changes in these zones may diminish mechanical performance, making them more susceptible to failure under tensile stresses, as indicated by material failures observed in static tensile tests.

This also means that regions with lower hardness can be potential mechanical failure points due to their reduced ability to withstand deformations and stresses. In the context of OWTs, this could translate into compromised structural stability, particularly when subjected to dynamic loads and stresses encountered in offshore environments. The execution of more weld passes, necessitated by the increased thickness, leads to more heat energy input, which affects the hardness and the ductility of the material. A broader HAZ with varying hardness can introduce inconsistencies in the mechanical performance, impacting the overall reliability and lifespan of OWT structures.

5 | Distortion Results

Distortion is common in the welding of plates in the longitudinal and transverse directions, which can have a significant impact on the material performance. Distortion measurements were conducted by first conducting a 3D scanning of the welded plates using the GoScan50 optical scanner with a resolution of 0.5 mm and accuracy of 0.1 mm capable of scanning large areas such as the welded plates in this study. The scanner was first calibrated using a calibration plate, and the scanned dimensions were compared with the actual steel plate dimensions from multiple scans for validation. The scanner's performance was compared against the permissible tolerances stipulated in ISO 10360-8:2013 [69]. In addition, the surfaces, edges, and geometrical features were found to be consistent and accurate when compared with actual steel plates and nominal CAD geometry. The VXElements software [70] was used to create the surface mesh (STL format) for the scanned plates which were then imported into GOM Inspect software [71] to obtain the distortion angles in the transverse direction. The meshes from the scans of the welded plates were aligned with the nominal CAD for each of the 6-, 10-, 15-, and 20-mm welded plates to calculate the surface deviations. From the calculated surface deviations, the angular distortion in the longitudinal direction as well the axial misalignments were obtained from sections across the plates.

This distortion in Figure 9 occurs due to factors such as the plate's length, clamping strategy, high heat input during welding, and a large amount of WM. Although these factors were minimized, distortion was induced primarily due to the induced residual stress in the longitudinal and transverse distortions. This challenge is highly possible even in large-scale manufacturing and production, as a high number of plates are often rolled and welded. Notably, thinner welded plates of 6 and 10 mm exhibited bending, while the 15-mm plate showed a butterfly shape as well as the 20-mm plate. Also, the thinner plates showed higher distortion due to the lower stiffness. In OWT applications, axial misalignment in the weld is often more critical due to the monopile's shape, and it receives more comprehensive guidance. However, the shipbuilding standard [72] applicable to some offshore structures provides a relevant recommendation for shipbuilding, specifying that the maximum distortion in welded flat plates should be within 5 mm, with an allowable limit of 10 mm. Consequently, all measured distortions in this study fall well within the acceptable boundaries. It should be noted, however, that only a single set of experiments was conducted for each plate thickness without repetition, which represents a limitation of the study.

An angular distortion, defined as the angle from the center of the weld to the two ends in the lateral direction, was obtained

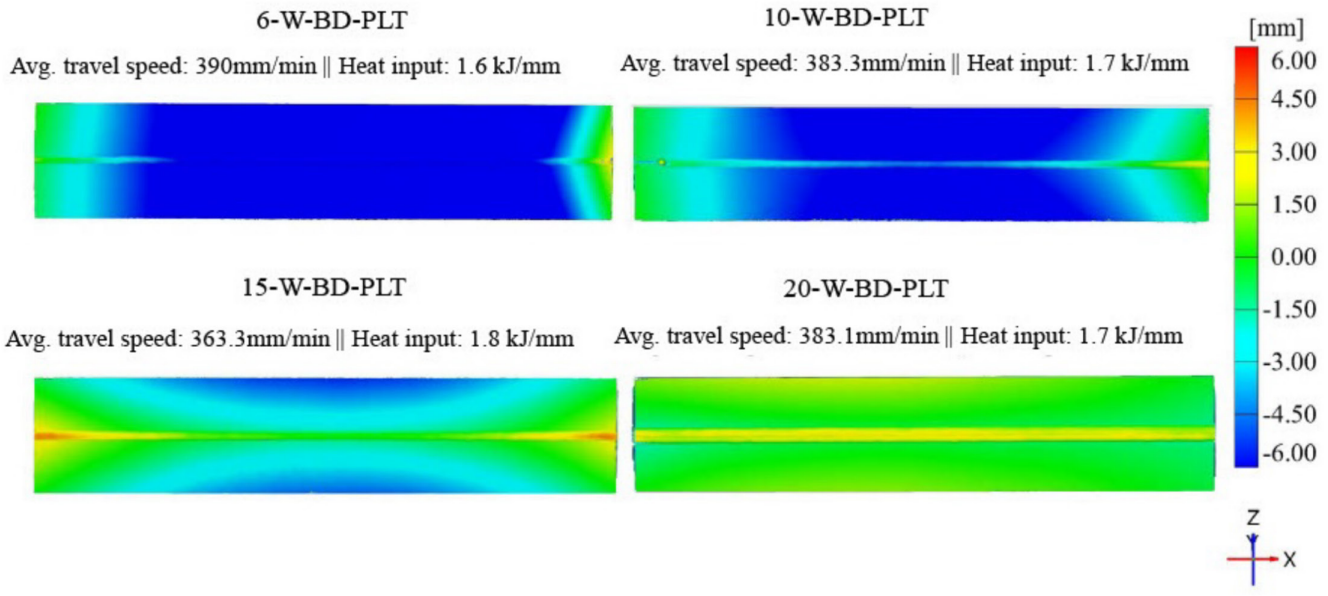

FIGURE 9 | Bending distortion values in vertical *y*-axis at the top surface of the plate. [Colour figure can be viewed at wileyonlinelibrary.com]

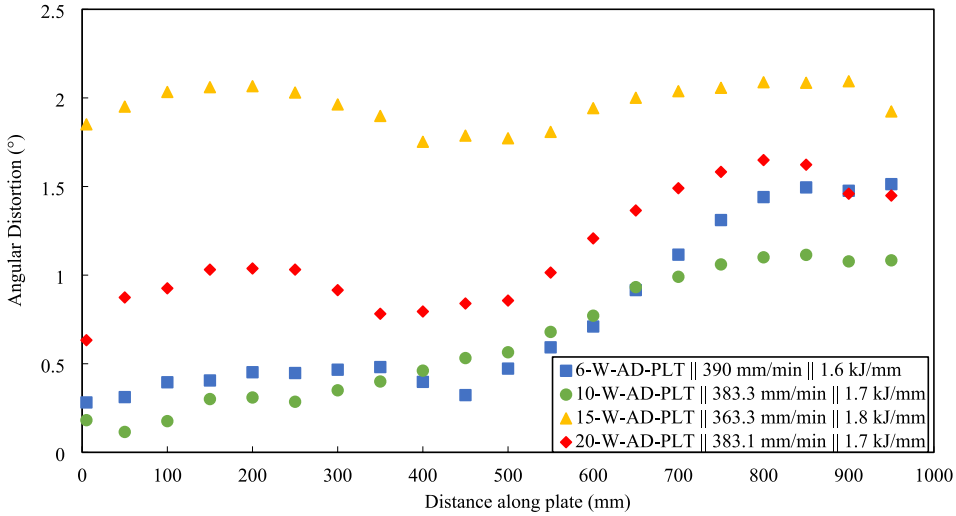

FIGURE 10 | Angular distortion along the plate. [Colour figure can be viewed at wileyonlinelibrary.com]

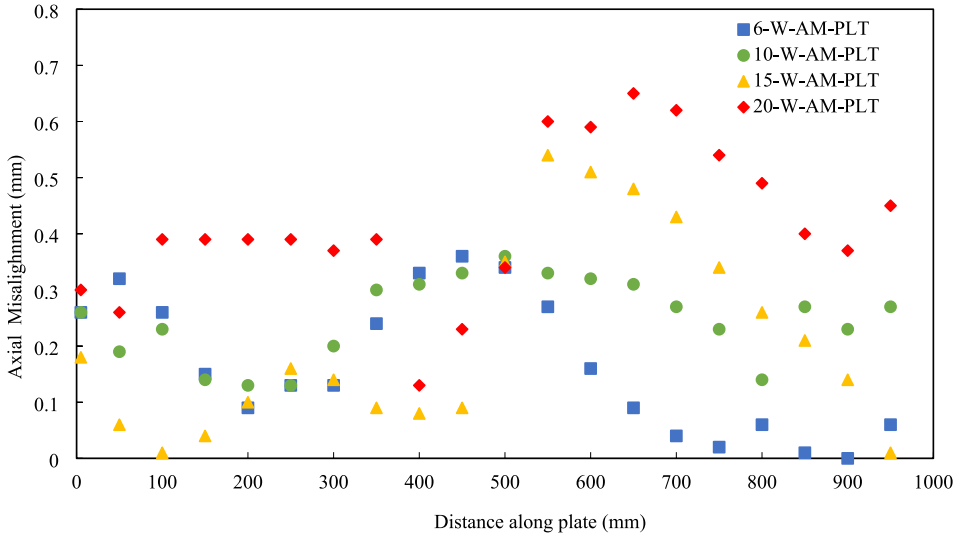

FIGURE 11 | Axial misalignment along the plate. [Colour figure can be viewed at wileyonlinelibrary.com]

and presented in Figure 10. It was observed that the angular distortion had the average highest values with the 15-mm welded plates due to the butterfly distortion mode. Also, due to its higher heat input (1.8 kJ/mm), it likely caused increased thermal expansion, leading to more pronounced distortion than in others. While travel speed and heat input values can affect the distortion [29], the influence of the thickness effect is observed in the material used in this study. Higher angular distortion values were observed towards the end of the plate, which is caused by the possible rebalancing of the residual stresses after unclamping and possibly because each weld pass has redistributed the residual stresses and affected the distortion. The angular distortion values for all plates at the end of the weld were observed to be higher than the recommended maximum of 1° in the B90 quality of the BS EN ISO 5817:2023 [73], which can affect the fatigue performance. The test specimens were selected from regions of the plate with an angular deviation of less than 1°, except for the 15 mm specimen. The 15-mm thick samples exhibited a stress magnification factor of 1.06, which is below the recommended threshold of 3. Therefore, they were deemed suitable for fatigue testing. Additional details regarding the impact are provided in Section 7.

Figure 11 shows the measurements of the axial misalignment of each plate thickness. On average, misalignment along the *x*-axis tends to worsen with increasing plate thickness, and it was most observable in the second half of the plate. However, the maximum value of 0.65 mm was attained for plates that were 20-mm thick. This value of axial misalignment is significantly lower than the 3 mm limit recommended by design standards for butt-welded plates [72–75]. Angular distortion and axial misalignment can lead to alterations in the geometry of the structure, causing an uneven load distribution. These changes can impact the fatigue performance of the structure, potentially reducing its fatigue life. The influence of distortion and misalignment is further discussed in Section 8.

From the observation above, some techniques are proposed for mitigating axial misalignment and angular distortion in welded S355G10 +M structural steel, which are critical for OWT and

shipbuilding applications. This includes prewelding simulations and design optimizations using computational welding mechanics and finite element analysis (FEA) for parameter optimization to minimize distortion, as well as controlled welding techniques like low heat input methods and strategic use of jigs and fixtures to limit thermal stress and mechanical misalignment as also observed in previous research [76–78]. Compliance with standards on weld quality guarantees conformity to permitted distortion limitations. A multidisciplinary approach that combines sophisticated technology, computational modeling, and material science can further enhance the performance of welded S355G10 +M structures and is crucial in maintaining the geometric tolerances required for large structures like OWT towers and foundations.

6 | Residual Stresses Results

The contour method is a comprehensive and destructive technique employed to assess and map the residual stresses in materials [79]. The S355G10 +M plates were cut using WEDM both across and along the weld (see Figure 3) for the 6-, 10-, 15-, and 20-mm thicknesses making a total of eight specimens. The cuts for specimens across the weld were taken at 100 mm from the end of the 330-mm × 200-mm plates (position in x direction). Subsequently, high-precision coordinate measuring machine (CMM) laser scanning technology using the Nikon noncontact laser scanners capable of measuring single point spacing of 22- and 1.8-µm accuracy was conducted. The validation of CMM laser measurements using ISO 10360-2:2009 [80] involves a step-by-step process. The CMM laser scanner was first calibrated in accordance with the protocols outlined in the standard, and a stable environment was chosen to facilitate the scanning process. A nominal CAD model of the specimens was constructed to ensure accurate representation. The specimens were scanned, and the acquired point cloud data were compared with the nominal CAD model. The deviations between the measured points and the model were computed and analyzed in the GOM software to identify potential regions of discrepancy between the measured and nominal geometries. The scanner's performance was thoroughly evaluated by contrasting the observed deviations against the permissible tolerances stipulated in ISO 10360-8:2013 [69] (maximum probing form error using 25 representative points in translatory scanning mode, maximum probing size error using all measured points in translatory scanning mode, and maximum probing dispersion value using 95% of the measured points in translatory scanning mode) to ensure accuracy. The validation workflow closely matches protocols used in residual stress investigations in S355 butt welds [81].

A surface mesh (STL format) was generated from the CMM data points, and it was then imported into the GOM software, where it was aligned to a flat surface. A smoothing was applied to the measured data points, but a negligible difference was observed, indicating that the CMM measurements were precisely taken as observed also in work measuring residual stress in a thick but-welded high-strength steel [82]. The displacements were first calculated in the GOM software. The measured displacements were converted in the opposite values (multiplied by −1), and then they were applied as a nodal displacement boundary condition in a FEA model using the default mapping in ANSYS mechanical. A static analysis was conducted using elastoplastic material properties. The material properties employed included a Young's modulus of 200 GPa, Poisson's ratio of 0.3, and stress–strain data from Section 3 to capture plasticity as it was inputted into the ANSYS material models isotropic hardening model. An element size of 1 mm produced from convergence studies and was applied in the model; the element type was a 3D structural solid element (SOLID185). An elastoplastic stress analysis was then performed, and the resulting back-calculated stresses on the cut surface derived from the FEA represented the residual stress component acting perpendicular to the cut plane. This FEA-based stress reconstruction technique is widely used in contour method studies involving welded joints [83].

The residual stresses across and along the welded specimens in the x and z directions were presented in Figures 12 and 13, respectively, for each thickness. In Figure 12, high tensile residual stresses are located in the WM region, while the highest compressive residual stresses were observed in the BM region of the specimens. In Figure 13, the highest tensile residual stresses are mostly observed close to the top of the WM. A comparison of the measurement results obtained across and along the weld revealed that the highest average tensile residual stresses across the weld (500 MPa) were significantly greater than those along the weld (with an average of 350 MPa). These values were in the range of the residual stresses obtained for similar materials [7, 18, 35, 84]. For all residual stress results, as thickness increased, the highest residual stress value also increased. This observation highlights a trend in residual stress magnitude relative to specimen thickness, as captured in the experimental measurements [85]. The contour method is destructive and resource-intensive, so single-specimen evaluations were conducted but well supported with detailed calibration and ISO-based accuracy validations. It should be noted that the single-specimen evaluation on the residual stresses in a single cut is limited to provide the full picture of the residual stress evolution along the plate for different thicknesses, but it provides valuable insight to its fatigue impact as discussed in Section 8.

In an OWT application of monopiles, the tensile stress results along the weld in Figure 13 are more relevant for fatigue because the direction of the stress (axial direction of the OWT) is the same as the induced stress from loading. The residual stresses across the weld in Figure 12 are relevant for applications where the hoop stresses are critical for material performance (e.g., pressure vessels and submarines).

Measured residual stresses can enhance yield strength but may also accelerate crack initiation and propagation, especially under corrosion-fatigue conditions. Effective management of residual stresses in welded structures, like offshore monopiles, is crucial for long-term reliability. Proper welding, stress-relief treatments, and regular inspection can help mitigate adverse impacts on structural integrity and service life.

7 | Fatigue Testing Results

Uniaxial fatigue tests were performed on the prepared dog-bone specimens using a 250-kN Instron servo-hydraulic testing machine. The stress range values applied in the uniaxial

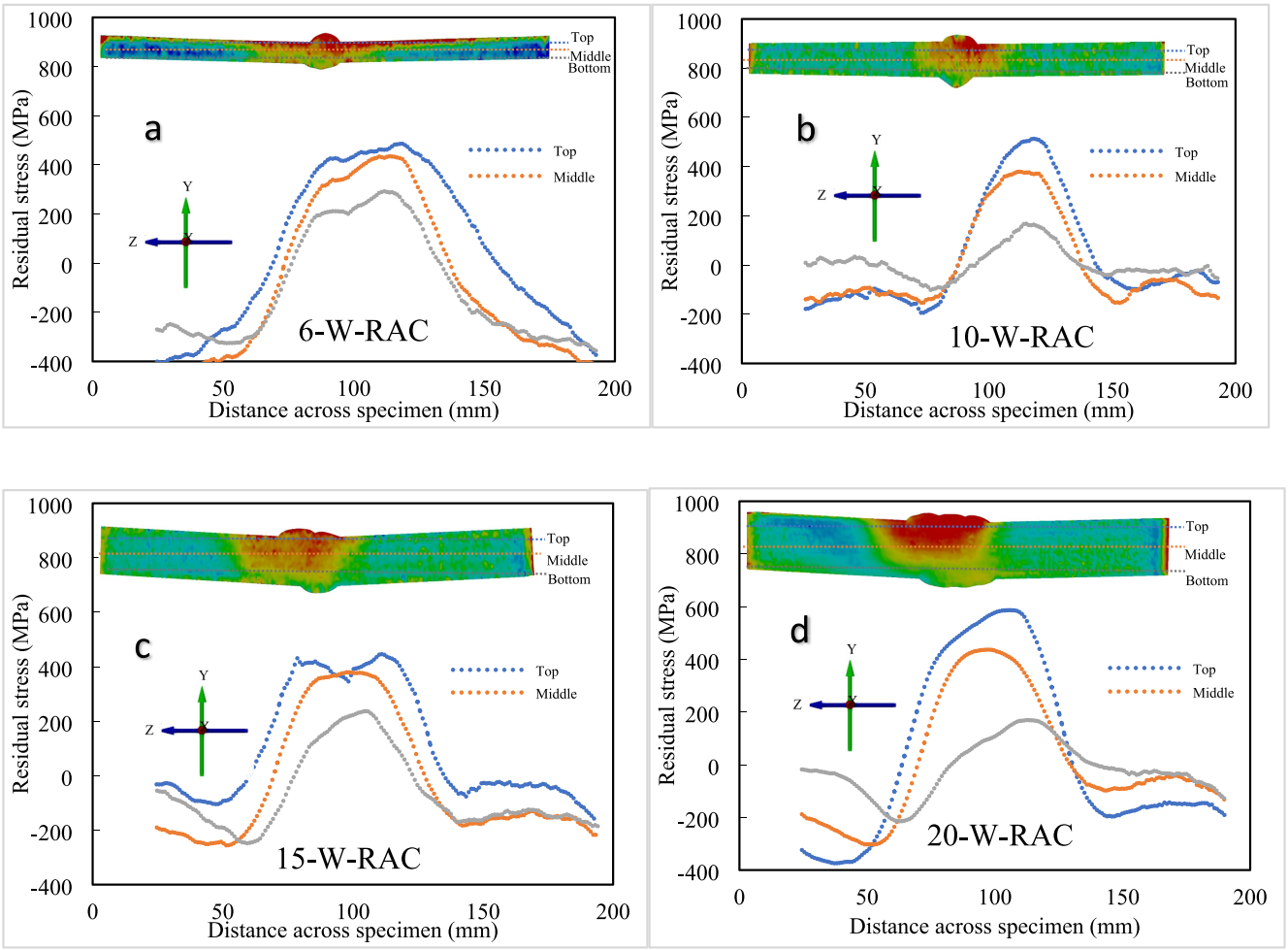

FIGURE 12 | Residual stress results across weld in x direction for (a) 6 mm, (b) 10 mm, (c) 15 mm, (d) 20 mm. [Colour figure can be viewed at wileyonlinelibrary.com]

fatigue tests were in the range of 150–300 MPa. All fatigue tests that were performed at a frequency of 10 Hz with a load ratio of $R = 0.5$ on dog-bone specimens were cut from sections of maximum of 0.2-mm misalignment and below which meets the butt weld criteria for Quality Level B according to BS EN ISO 5817:2023 [73]. The stress ranges were selected to avoid fracture failure due to reaching the ultimate strength of the material. The decision to use a stress ratio of 0.5 in the fatigue testing primarily stems from the desire to replicate the operational conditions in the tension–tension regime to which offshore structures are exposed. These structures consistently experience tensile loads due to wind and waves. Another rational is to account for the residual stresses induced in the weld of offshore structures which act as a mean stress. Additionally, employing a stress ratio of 0.5 aligns with standard testing protocols and design codes (DNV, IIW fatigue design standard for welded joints [75, 86]), ensuring compliance and relevance in the examination of fatigue behaviors. The fatigue tests were monitored using a camera to determine the exact location of the crack initiation and crack propagation stage, and nonwelded specimens were tested for calibration for each thickness. The number of cycles to failure obtained from uniaxial fatigue tests was correlated with the applied stress range in log–log axes, and the indicative S–N curves are presented in Figure 14. In this figure, the number of cycles to failure was observed at a cycle range of $10^4 - 10^6$ with a fatigue strength in the range of 120–234 MPa across the four thicknesses. The fatigue results of the S355G10 +M specimens were also compared to the provisions of the FAT Class 90 in air [86], Class D specification for air. Also, thickness correction factor has been included in Figure 14 according to the fatigue design standard [75, 86] based on 25-mm reference thickness and fatigue exponent of 0.25.

Results from Figure 14 indicate that the S355G10 +M specimens were in alignment with the design codes in estimating fatigue life for structural steel used in monopiles. The results show that the test barely exceeds the FAT90 and D-curve with similar results obtained for another grade of S355 SAW butt-welded steel fatigue results [12]. The considered fatigue strengths at two million cycles across 6- to 20-mm specimens were observed to be in the range of 96–128 MPa. The experiments showed that the thickness effect on a butt-welded S355G10 +M specimen under uniaxial fatigue was not very strong, but the trend of decreasing fatigue strength by increasing thickness was observed. The results obtained in this study verify the hypothesis from a conducted review of thickness effects on fatigue in butt-welded joints that thickness has no pronounced effect on fatigue strength [87]. Residual stress and misalignment have been found to contribute more to the thickness effects in another study [12],

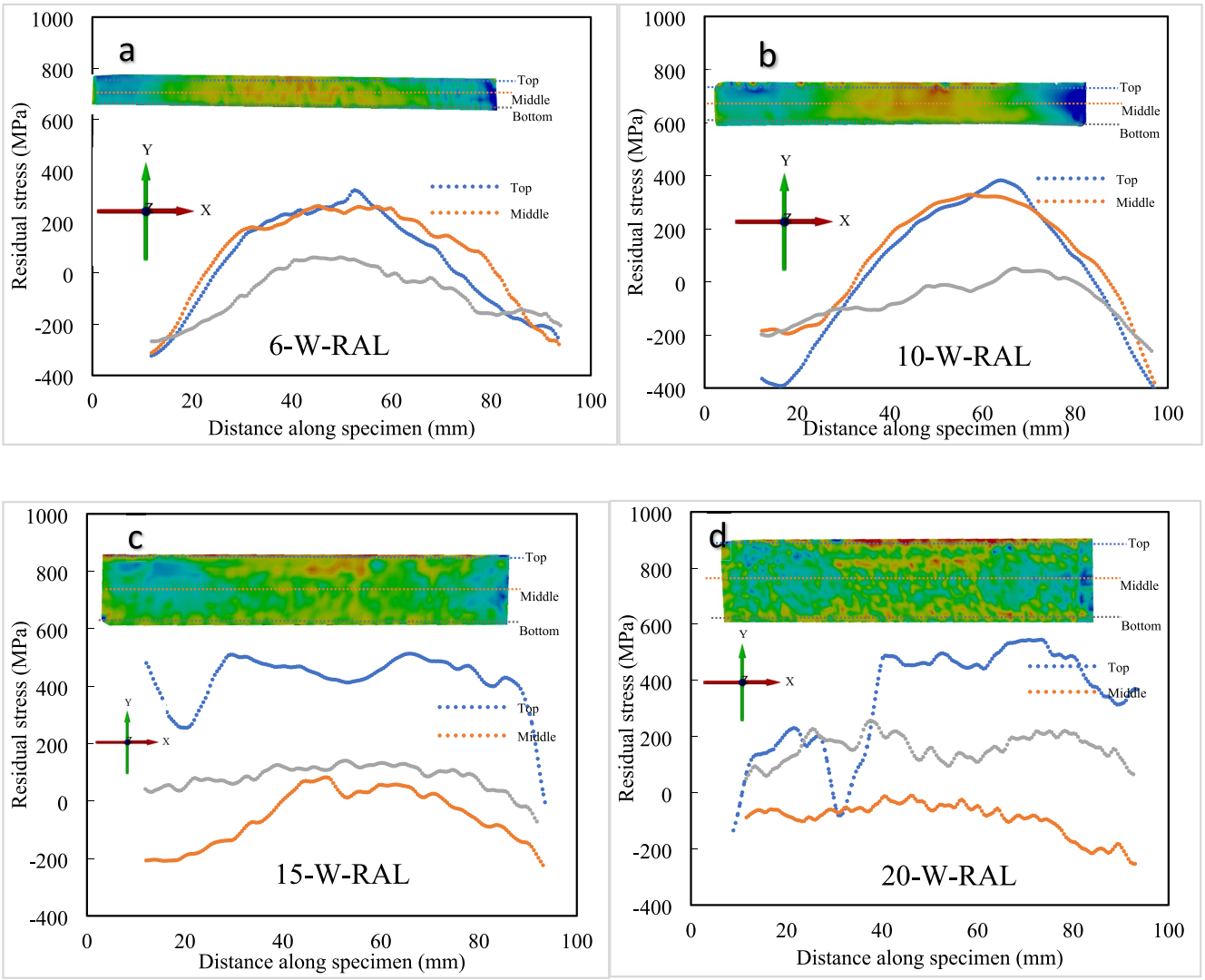

FIGURE 13 | Residual stress results along weld in z direction for (a) 6 mm, (b) 10 mm, (c) 15 mm, (d) 20 mm. [Colour figure can be viewed at wileyonlinelibrary.com]

in particular for the 15 thick samples where the angular deviation was measured to be greater than 1° due to distortion. The calculated stress magnification factors and residual stress trends across thicknesses have a contribution for the reduced fatigue strength. This is particularly true for the 15-mm thick specimens where the S–N data show the greatest scatter indicating that the stress magnification factor due to distortion might have an impact. This indicates that the thickness effect should be analyzed more holistically by analyzing residual stresses, misalignment, and stress concentrations. The crack initiation stage, crack propagation stage, and fracture stage were all visible in the fractured specimens that resulted from cyclic loading. Like most uniaxial fatigue tests, the fatigue cracks propagated in a plane perpendicular to the first principal stress. The subtle transition region between the crack propagation and the unstable fracture is a stable fatigue crack growth region. This suggests that the nominal stresses were quite high. The macroscopic shape of the fragmented surface (shown in Figure 15) provides further evidence that the specimen failed due to plastic collapse.

For corrosive environments, a benchmark against the same grade of steel S355J2+N is considered. It has average yield and ultimate tensile stress of 454 and 556 MPa [18, 88] comparable to Table 1. The 6-mm S355G10 +M samples tested in air demonstrated the highest fatigue life at 2 million cycles, with the predicted fatigue life for 4-mm S355J2+N under corrosion-fatigue conditions at $R=0.5$ being significantly lower, with 65%–70% reduction in fatigue life due to environmental effects alone. This significant drop in fatigue resistance under corrosive loading is consistent with findings [17]. A similar trend was observed in the 20 mm S355G10 +M specimens, where the 20-mm S355J2+N corrosion-fatigue sample in air and seawater was lower. The 20-mm S355J2+N corrosion-fatigue life at $R=0.5$ in air consistently lies beneath the S355G10 +M 20-mm data across the full stress range. The DNV-C203 seawater curve shows an even steeper drop-off in fatigue life, highlighting the severity of corrosion-fatigue conditions in offshore structural fatigue assessments [2, 3, 11].

These comparisons reinforce two key findings: S355G10 +M performs robustly under standard fatigue conditions, particularly in thinner sections where residual stress effects are less pronounced, and corrosion-fatigue can reduce fatigue life by more than 60%, even at moderate stress ranges. The results also

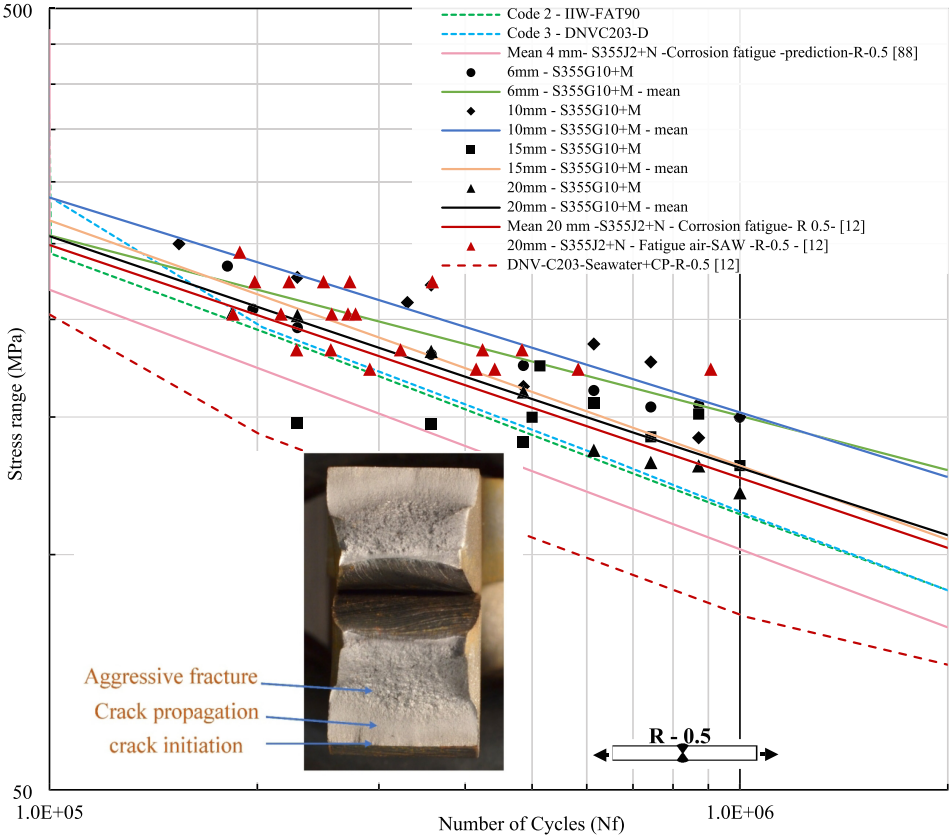

FIGURE 14 | S–N curve for as-welded S355G10 +M structural steel and comparison to corrosion fatigue welded S355J2+N specimens with machined weld faces with eliminated stress concentrations. [Colour figure can be viewed at wileyonlinelibrary.com]

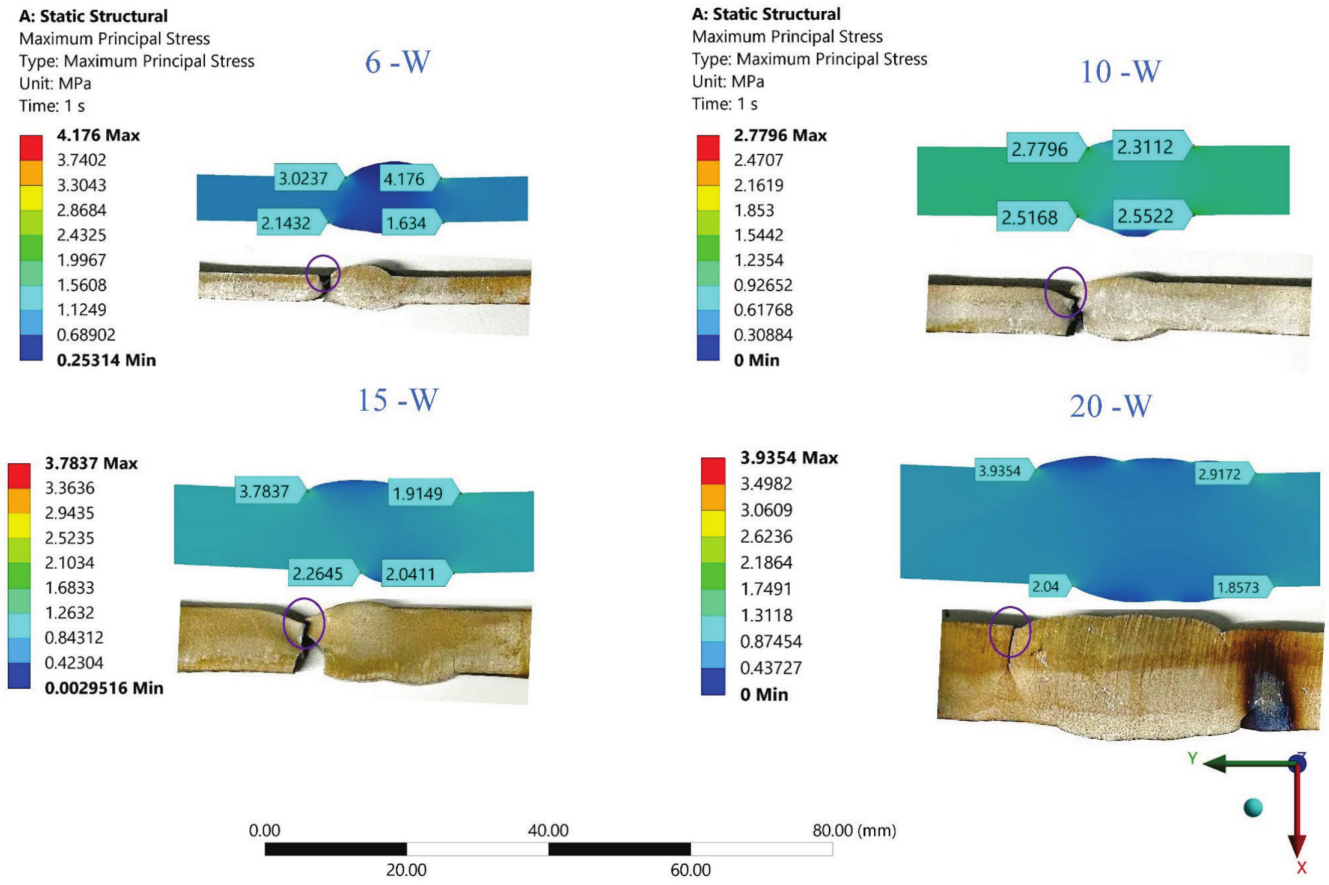

FIGURE 15 | Predicted SCF and failure modes of welded S355G10 +M specimens. [Colour figure can be viewed at wileyonlinelibrary.com]

show that air-tested 6-mm S355G10 +M outperforms the 20-mm corrosion-fatigue curves of S355J2+N, indicating that both thickness and environmental exposure could influence design decisions for offshore structural components. Thus, while this study experimentally tested fatigue in standard environments, the inclusion of literature-based corrosion-fatigue data provides a meaningful benchmark for offshore application.

8 | Influence of Stress Concentration, Distortion, and Residual Stress on Fatigue

Stress concentration can influence fatigue due to localized stresses induced by notches in the weld. This was investigated using a 2D plane strain finite element model. The geometry was determined from the surface mesh from the CMM data points. The mesh was constructed with quadratic 8-node elements. All modeled notches were sectioned into partitions of 1 mm for mesh, with edge sizing element size of 0.1 mm from convergence studies applied. Rounded corners were ensured to avoid stress singularity at very sharp notches. The material properties employed included a Young's modulus of 200 GPa and Poisson's ratio of 0.3. A nominal stress of 1 MPa was applied uniformly on one end, and a fixed boundary condition was applied on the opposite end. In these analyses, the maximum principal stresses are used to determine the stress concentration values. The maximum principal stresses are dominated by the nominal stress in the direction of the applied load.

The results are presented in Figure 15, where the SCF between the HAZ and WM (weld toe) is shown to range between 2.8 and 4.2. The highest SCF values when compared with fatigue-fractured specimens showed that these were indeed regions of crack initiation and propagation under cyclic loading except for the 6-mm thickness where the crack initiated at weld toe that had a SCF of 3 in the simulation. This can be explained with that fact that the SCF is just one of the factors in the notch. Other factors are the notch size and the surface roughness at the notch [88]. These points confirm the local stress control of fatigue initiation. Another observation is that the SCF at the location of crack initiation and growth for the 15- and 20-mm-thick samples is 3.78 and 3.93, respectively, while for the 6- and 10-mm thicknesses, the SCFs are 3.02 and 2.78, respectively. The higher SCFs for the 15- and 20-mm thicknesses can explain the lower fatigue strength from Figure 14 for these thicknesses compared to 6 and 15 mm. These results show the impact of local stresses and notch morphology, especially with welds often not machined in the actual installation of monopiles.

The scale effect was observed although not significant across the range of thicknesses tested. As thickness increased, fatigue strength seemed to decrease partly due to higher residual stress retention and SCFs and also due to increased defect volume and lower stress gradients across the section. These size-related effects have been reported in other studies on thick welded structural steels [89, 90].

To assess the defect population responsible for crack initiation, a macrostructural inspection of the welded S355G10 +M specimens in Figure 7 revealed no major welding flaws such as porosity clusters, lack of fusion, or hot cracks indicating high weld integrity. However, the minor etching pores observed in the HAZ for15- and 20-mm-thick samples could serve as potential initiation sites for fatigue cracks under cyclic loading and contribute to why they had lower fatigue strength in Figure 14. These pores represent microstructural imperfections likely caused by gas entrapment or localized overheating during multipass weld passes. Though small and isolated, such HAZ-based microdefects can significantly influence early-stage crack nucleation, especially in high-stress regions near weld toes where stress concentration factors (SCFs) are elevated. This observation complements the SCF results (Figure 15).

Apart from the influence of residual stresses and SCF on the fatigue strength of S355G10 +M, misalignment and distortion in the butt-welded joint under axial loading were observed to induce only minimal additional bending stresses that have conservatively not been incorporated into the SN curve in Figure 14. This causes a small increase in stress on one of the two surfaces within the welded region, which leads to a slightly higher overall stress in specific areas. The effect of these geometrical imperfections minimally intensified the stresses observed during fatigue testing. The misalignment and angular distortion stress magnification factors have previously been established based on global and local stress effects [75, 86], and they have been combined as stress magnification factors [12]. The axial ($K_{m\text{-}axial}$) and angular ($K_{m\text{-}ang}$) stress magnification factors can be expressed by the following [12]:

$$K_{m-axial} = 1 + 3\,\frac{e}{t} \tag{1}$$

$$K_{m-ang} = 1 + \frac{3}{4}\alpha\frac{L}{t} \tag{2}$$

where e is the axial misalignment, t is the plate thickness, α is the angular distortion, and L is the distance between the fixing points of the plates. The total stress magnification factor (K_{m_T}) can be given by the following [12]:

$$K_{m\_T} = 1 + \left(K_{m-axial} - 1\right) + \left(K_{m-ang} - 1\right) \tag{3}$$

Unless the total stress magnification factor exceeds 1.3, axial and angular misalignments do not significantly reduce fatigue strength in joints subjected to axial stresses [91]. The total stress magnification factor (Equation 3) from angular distortion and axial misalignments was calculated to be 1.09, 1.08, 1.06, and 1.06 for 6-, 10-, 15-, and 20-mm-thick plates, respectively. This showed that while fatigue strength was not substantially reduced as the calculated total stress magnification factors were less than 1.3 [91], the increase in thickness reduced the effect of the secondary bending stresses. Thus, in addition to the SCF effect on fatigue life, misalignments and distortion can be a contributing factor for the material performance of S355G10 +M.

As shown in Figure 13, tensile residual stresses increase with thickness, with values reaching up to 500 MPa in the 20-mm specimen compared to approximately 320 MPa in the 6-mm plate. These residual stresses are aligned with the axial loading direction that promotes crack opening, thereby reducing the effective fatigue strength. The contour method measures these stresses by recording surface displacements caused by elastic release when the specimen is cut and applies reverse displacement to estimate precut

residual stresses. The measured residual stresses, combined with the stress ratio, represent the mean stress effect, which is known to reduce fatigue strength. Figure 14 further supports this trend, where the number of cycles to failure decreased with increasing plate thickness under the same stress ratio ($R = 0.5$). This could be due to differences in stress distribution across thicknesses; while the cutting process releases residual stresses, thicker samples may retain higher residual stresses in the midsection compared to thinner samples. These measured residual stresses contribute to the mean stress effect observed in fatigue performance, particularly under positive stress ratios. This is consistent with prior findings [7, 17], where tensile residual stresses were shown to reduce fatigue life in welded S355 and S355G10 +M plates. This also explains the practical approach to use a stress ration of $R = 0.5$ when samples are tested to account for the residual stresses locked in the material as measured and demonstrated in Section 6. Alternative approach is to conduct fatigue testing at $R = -1$ while incorporating the effect of residual stresses more dynamically. Rather than adding residual stresses as a fixed mean stress using the Goodman approach, a modified S–N curve that accounts for residual stress relaxation under cyclic loading would provide a more accurate fatigue life prediction. This approach considers the interaction between external loads and residual stresses, better reflecting realistic fatigue behavior in welded joints. In contrast to how the residual stresses are accounted into fatigue assessments, the total effect of the SCF, notch size, surface roughness at the notch, misalignment, and angular distortions can be accounted in the S–N curve by conducting a fatigue test on samples.

The comprehensive examination of submerged arc-welded S355G10 +M plates of varying thicknesses revealed critical insights into weld quality, mechanical properties, and fatigue life, emphasizing the steel's suitability for high-capacity offshore constructions in marine environments. Analyzing the plate thickness effects and SCFs provided pragmatic guidance for the design and manufacture decision of future OWTs and marine structures. While this study sheds light on the material performance of S355G10 +M for offshore wind monopiles, it was limited to a specific range of plate thicknesses (6, 10, 15, and 20 mm) compared to practical applications, where thicknesses can reach 90 mm. Future research is encouraged to include a larger range of thicknesses, further improving the understanding of material performance of S355G10 +M.

9 | Conclusions

This study sheds light on the material performance of submerged arc-welded S355G10 +M structural steel in high-capacity OWTs, considering hardness, distortion, residual stress, and fatigue. The innovative focus is the investigation of the mechanical properties and plate thickness effects applicable to OWT tower and monopile and marine structures, with insights that could significantly impact the design and manufacture of more efficient and resilient OWTs. The study's findings are summarized below:

1. The SAW process was on S355G10+M plates of different thicknesses using a double V-groove and multi-pass approach allowed for a weld quality which met the standards required for OWT monopiles.
2. Static tensile test specimens were fractured in the base material, indicating stronger weld material. Welded specimens exhibited slightly lower yield strength but higher ultimate strength with reduced plastic deformation capacity and lower ductility across all thicknesses.
3. Hardness increased with plate thickness and the base material (BM) and heat-affected zone (HAZ) identified was a potential weak point where material failure occurred under tensile loading due to microstructural changes.
4. Distortion measurements showed that axial misalignment and angular distortion were in acceptable limits; thinner 6- and 10-mm plates showed bending deformation, while the 15 and 20-mm-thick plates showed a butterfly deformation shape.
5. Significant tensile residual stresses at the weld toe increased with thickness and should be accounted for in S–N curves or fatigue tests of samples at higher stress ratios (e.g., $R = 0.5$).
6. All tested samples failed at the weld toe due to stress concentration. Weld grinding can improve fatigue performance, though corrosion-induced pits present another source of stress concentration in marine environments.
7. Fatigue life of butt-welded S355G10+M specimens was greater than industrial code-based strength predictions. Used fatigue codes and postprocessing technologies such as machining the weld, heat treatment, and surface hardening can further enhance fatigue performance, confirming suitability for offshore and marine applications.

Author Contributions

Victor Okenyi: writing, conceptualization, methodology, analysis, software. **Shukri Afazov:** editing, theory, analysis, supervision. **Neil Mansfield:** supervision. **Jeyaganesh Balakrishnan:** reviewing, testing. **William Kyffin:** testing, software. **Petros Siegkas:** reviewing, supervision. **Tiziana Marrocco:** testing, software. **Mahdi Bodaghi:** reviewing, supervision.

Acknowledgments

The authors have nothing to report.

Conflicts of Interest

The authors declare no conflicts of interest.

Data Availability Statement

All data that support the findings of this study are included in this study.

References

1. British Standards Institution, "10025–2: 2019: Hot Rolled Products of Structural Steels. Part 2-Technical Delivery Conditions for Non-Alloy Structural Steels," (2019).

2. V. Igwemezie, A. Mehmanparast, and A. Kolios, "Materials Selection for XL Wind Turbine Support Structures: A Corrosion-Fatigue Perspective," *Marine Structures* 61 (2018): 381–397.

3. V. Okenyi, M. Bodaghi, N. Mansfield, S. Afazov, and P. Siegkas, "A Review of Challenges and Framework Development for Corrosion

Fatigue Life Assessment of Monopile-Supported Horizontal-Axis Offshore Wind Turbines," *Ships and Offshore Structures* 19 (2022): 1–15.

4. V. Okenyi, M. Bodaghi, P. Siegkas, N. Mansfield, and S. Afazov, "Stress Analyses of High-Rated Capacity Large Diameter Offshore Wind Turbines: Analytical and Numerical Analyses of Uniform Corrosion Effects," *Proceedings of the Institution of Mechanical Engineers, Part C: Journal of Mechanical Engineering Science* 238 (2023): 09544062231208551.

5. American Society for Testing Materials, "ASTM E8/E8M-22: Standard Test Methods for Tension Testing of Metallic Materials," 03.01, (2022).

6. M. Sokolov, A. Salminen, M. Kuznetsov, and I. Tsibulskiy, "Laser Welding and Weld Hardness Analysis of Thick Section S355 Structural Steel," *Materials and Design* 32 (2011): 5127–5131.

7. A. Jacob, J. Oliveira, A. Mehmanparast, F. Hosseinzadeh, J. Kelleher, and F. Berto, "Residual Stress Measurements in Offshore Wind Monopile Weldments Using Neutron Diffraction Technique and Contour Method," *Theoretical and Applied Fracture Mechanics* 96 (2018): 418–427.

8. A. Singh and R. P. Singh, "A Review of Effect of Welding Parameters on the Mechanical Properties of Weld in Submerged Arc Welding Process," *Materials Today Proceedings* 26 (2019): 1714–1717.

9. M. Braun, "Statistical Analysis of Sub-Zero Temperature Effects on Fatigue Strength of Welded Joints," *Welding in the World* 66 (2022): 159–172.

10. T. Köder and B. Bohlmann, "Experimental Fatigue Analysis of Butt-Welded Joints," *Ship Technology Research* 61 (2014): 132–141.

11. S. Gkatzogiannis, J. Weinert, I. Engelhardt, P. Knoedel, and T. Ummenhofer, "Correlation of Laboratory and Real Marine Corrosion for the Investigation of Corrosion Fatigue Behaviour of Steel Components," *International Journal of Fatigue* 126 (2019): 90–102.

12. Ó. M. Ólafsson and C. Berggreen, "Improved Design Basis of Welded Joints in Seawater," DTU Mechanical Engineering, (2016).

13. A. Ohta, N. Suzuki, and Y. Maeda, "Shift of S-N Curves With Stress Ratio," *Welding in the World* 47 (2003): 19–24.

14. K. Kanishka and B. Acherjee, "A Systematic Review of Additive Manufacturing-Based Remanufacturing Techniques for Component Repair and Restoration," *Journal of Manufacturing Processes* 89 (2023): 220–283.

15. A. M. P. De Jesus, R. Matos, B. F. C. Fontoura, C. Rebelo, L. Simões Da Silva, and M. Veljkovic, "A Comparison of the Fatigue Behavior Between S355 and S690 Steel Grades," *Journal of Constructional Steel Research* 79 (2012): 140–150.

16. J. Li, S. Nie, H. Kou, M. Elchalakani, X. Yu, and G. Dai, "Static and Fatigue Properties of 80 mm-Thick Q460GJC Butt Weld Joint," *Journal of Constructional Steel Research* 184 (2021): 106809.

17. H. Xin and M. Veljkovic, "Residual Stress Effects on Fatigue Crack Growth Rate of Mild Steel S355 Exposed to Air and Seawater Environments," *Materials and Design* 193 (2020): 108732.

18. A. Jacob, A. Mehmanparast, R. D'Urzo, and J. Kelleher, "Experimental and Numerical Investigation of Residual Stress Effects on Fatigue Crack Growth Behaviour of S355 Steel Weldments," *International Journal of Fatigue* 128 (2019): 105196.

19. P. J. Withers and H. K. D. H. Bhadeshia, "Residual Stress. Part 1 – Measurement Techniques," *Materials Science and Technology* 17 (2001): 355–365.

20. A. Khajeian, A. H. Mahmoudi, and A. Mehmanparast, "Shot Peening Effects on Residual Stresses Redistribution of Offshore Wind Monopile Multi-Pass Weldments," *Marine Structures* 66 (2019): 106–120.

21. P. K. Taraphdar, R. Kumar, A. Giri, C. Pandey, M. M. Mahapatra, and K. Sridhar, "Residual Stress Distribution in Thick Double-V Butt Welds With Varying Groove Configuration, Restraints and Mechanical Tensioning," *Journal of Manufacturing Processes* 68 (2021): 1405–1417.

22. Y. Zhang, X. Liu, Y. Zhou, and Y. Shi, "Influence of Welding Method on Residual Stress and Metallography of a Mild Steel Welded Butt-Joint Plate," *Journal of Constructional Steel Research* 199 (2022): 107640.

23. A. K. Mondal, P. Biswas, and S. Bag, "Prediction of Welding Sequence Induced Thermal History and Residual Stresses and Their Effect on Welding Distortion," *Welding in the World* 61 (2017): 711–721.

24. Y. H. P. Manurung, R. N. Lidam, M. R. Rahim, et al., "Welding Distortion Analysis of Multipass Joint Combination With Different Sequences Using 3D FEM and Experiment," *International Journal of Pressure Vessels and Piping* 111–112 (2013): 89–98.

25. H. Long, D. Gery, A. Carlier, and P. G. Maropoulos, "Prediction of Welding Distortion in Butt Joint of Thin Plates," *Materials and Design* 30 (2009): 4126–4135.

26. A. A. Bhatti, Z. Barsoum, H. Murakawa, and I. Barsoum, "Influence of Thermo-Mechanical Material Properties of Different Steel Grades on Welding Residual Stresses and Angular Distortion," *Materials & Design (1980–2015)* 65 (2015): 878–889.

27. T. Urbański and M. Taczała, "Prediction of the Welding Distortions of Butt Welded Joints Using Total Moments Method Based on Equivalent Loads," *Journal of Manufacturing Processes* 75 (2022): 1039–1057.

28. C. Rubio-Ramirez, D. F. Giarollo, J. E. Mazzaferro, and C. P. Mazzaferro, "Prediction of Angular Distortion due GMAW Process of Thin-Sheets Hardox 450® Steel by Numerical Model and Artificial Neural Network," *Journal of Manufacturing Processes* 68 (2021): 1202–1213.

29. P. C. Adamczuk, I. G. Machado, and J. A. E. Mazzaferro, "Methodology for Predicting the Angular Distortion in Multi-Pass Butt-Joint Welding," *Journal of Materials Processing Technology* 240 (2017): 305–313.

30. L. Li, H. Xia, N. Ma, B. Pan, Y. Huang, and S. Chang, "Comparison of the Welding Deformation of Mismatch and Normal Butt Joints Produced by Laser-Arc Hybrid Welding," *Journal of Manufacturing Processes* 34 (2018): 678–687.

31. Y. Zhang, Q. Wang, and Y. Liu, "Adaptive Intelligent Welding Manufacturing," *Welding Journal* 100 (2021): 63–83.

32. R. Yu, Y. Cao, H. Chen, Q. Ye, and Y. Zhang, "Deep Learning Based Real-Time and In-Situ Monitoring of Weld Penetration: Where We Are and What Are Needed Revolutionary Solutions?," *Journal of Manufacturing Processes* 93 (2023): 15–46.

33. Y. Wang, G. Feng, X. Pu, and D. Deng, "Influence of Welding Sequence on Residual Stress Distribution and Deformation in Q345 Steel H-Section Butt-Welded Joint," *Journal of Materials Research and Technology* 13 (2021): 144–153.

34. C. Liu, C. Lin, J. Wang, et al., "Residual Stress Distributions in Thick Specimens Excavated From a Large Circular Wire+arc Additive Manufacturing Mockup," *Journal of Manufacturing Processes* 56 (2020): 474–481.

35. Q. Wang, Y. Zhao, T. Zhao, D. Yan, G. Wang, and A. Wu, "Influence of Restraint Conditions on Residual Stress and Distortion of 2219-T8 Aluminum Alloy TIG Welded Joints Based on Contour Method," *Journal of Manufacturing Processes* 68 (2021): 796–806.

36. X. Liu, K. F. Chung, M. Huang, G. Wang, and D. A. Nethercot, "Thermomechanical Parametric Studies on Residual Stresses in S355 and S690 Welded H-Sections," *Journal of Constructional Steel Research* 160 (2019): 387–401.

37. H. Xin, J. A. F. O. Correia, M. Veljkovic, F. Berto, and L. Manuel, "Residual Stress Effects on Fatigue Life Prediction Using Hardness Measurements for Butt-Welded Joints Made of High Strength Steels," *International Journal of Fatigue* 147 (2021): 106175.

38. V. Igwemezie, P. Dirisu, and A. Mehmanparast, "Critical Assessment of the Fatigue Crack Growth Rate Sensitivity to Material Microstructure

in Ferrite-Pearlite Steels in Air and Marine Environment," *Materials Science and Engineering A* 754 (2019): 750–765.

39. S. Anandavijayan, A. Mehmanparast, J. Braithwaite, F. Brennan, and A. Chahardehi, "Material Pre-Straining Effects on Fatigue Behaviour of S355 Structural Steel," *Journal of Constructional Steel Research* 183 (2021): 106707.

40. S. Suresh, *Fatigue of Materials* (Cambridge University Press, 1992).

41. W. Dong, T. Moan, and Z. Gao, "Fatigue Reliability Analysis of the Jacket Support Structure for Offshore Wind Turbine Considering the Effect of Corrosion and Inspection," *Reliability Engineering and System Safety* 106 (2012): 11–27.

42. D. Ancona and J. M. Wind, *Wind Turbine - Materials and Manufacturing Fact Sheet*, vol. 19 (Princeton Energy Resources International, LLC, 2001).

43. R. Melchers, "A Review of Trends for Corrosion Loss and Pit Depth in Longer-Term Exposures," *Corrosion and Materials Degradation* 1, no. 1 (2018): 42–58.

44. S. J. Price and R. B. Figueira, "Corrosion Protection Systems and Fatigue Corrosion in Offshore Wind Structures: Current Status and Future Perspectives," *Coatings* 7 (2017): 1–51.

45. V. Igwemezie and A. Mehmanparast, "Waveform and Frequency Effects on Corrosion-Fatigue Crack Growth Behaviour in Modern Marine Steels," *International Journal of Fatigue* 134 (2020): 105484.

46. V. Igwemezie, A. Mehmanparast, and A. Kolios, "Current Trend in Offshore Wind Energy Sector and Material Requirements for Fatigue Resistance Improvement in Large Wind Turbine Support Structures—A Review," *Renewable and Sustainable Energy Reviews* 101 (2019): 181–196.

47. A. Mehmanparast, O. Adedipe, F. Brennan, and A. Chahardehi, "Welding Sequence Effects on Residual Stress Distribution in Offshore Wind Monopile Structures," *Frattura ed Integrità Strutturale* 10 (2016): 125–131.

48. J. Velarde and E. E. Bachynski, "Design and Fatigue Analysis of Monopile Foundations to Support the DTU 10 MW Offshore Wind Turbine," *Energy Procedia* 137 (2017): 3–13.

49. E. Gaertner, J. Rinker, and L. Sethuraman, "IEA Wind TCP Task 37: Definition of the IEA 15-Megawatt Offshore Reference Wind Turbine," (2020).

50. DNV G, "DNV-OS-B101: Offshore Standard, Metallic Materials," (2009).

51. British Standards Institution, "BS EN ISO 23277:2015: Non-Destructive Testing of Welds. Penetrant Testing. Acceptance Levels," (2015).

52. British Standards Institution, "BS EN 1011–2:2001: Welding. Recommendations for Welding of Metallic Materials. Arc Welding of Ferritic Steels," (2001).

53. O. Adedipe, F. Brennan, and A. Kolios, "Review of Corrosion Fatigue in Offshore Structures: Present Status and Challenges in the Offshore Wind Sector," *Renewable and Sustainable Energy Reviews* 61 (2016): 141–154.

54. A. Mehmanparast, F. Brennan, and I. Tavares, "Fatigue Crack Growth Rates for Offshore Wind Monopile Weldments in Air and Seawater: SLIC Inter-Laboratory Test Results," *Materials and Design* 114 (2017): 494–504.

55. British Standards Institution, "BS EN ISO 6506-1:2014: Metallic Materials. Brinell Hardness Test. Test Method," (2014).

56. The MathWorks Inc, "Statistics and Machine Learning Toolbox," (2022).

57. V. Igwemezie, A. Mehmanparast, and F. Brennan, "The Role of Microstructure in the Corrosion-Fatigue Crack Growth Behaviour in Structural Steels," *Materials Science and Engineering A* 803 (2021): 140470.

58. V. V. Knysh, B. N. Mordyuk, S. O. Solovei, Y. P. Volosevich, M. A. Skoryk, and D. A. Lesyk, "Combining Electric Discharge Surface Alloying and High-Frequency Mechanic Impact Post-Processing for Increased Corrosion Fatigue Life of As-Welded Transverse Non-Load-Carrying Attachments of the S355 Steel," *International Journal of Fatigue* 177 (2023): 107926.

59. G. R. Mirshekari, E. Tavakoli, M. Atapour, and B. Sadeghian, "Microstructure and Corrosion Behavior of Multipass Gas Tungsten Arc Welded 304L Stainless Steel," *Materials and Design* 55 (2014): 905–911.

60. X. Zhang, S. Zheng, and X. Zhao, "Experimental and Numerical Investigations Into Seismic Behavior of Corroded Steel Frame Beams and Columns in Offshore Atmospheric Environment," *Journal of Constructional Steel Research* 201 (2023): 107757.

61. A. A. Olajire, "Recent Advances on Organic Coating System Technologies for Corrosion Protection of Offshore Metallic Structures," *Journal of Molecular Liquids* 269 (2018): 572–606.

62. M. Abbas and M. Shafiee, "An Overview of Maintenance Management Strategies for Corroded Steel Structures in Extreme Marine Environments," *Marine Structures* 71 (2020): 102718.

63. E. Meyer, "Untersuchungen über härteprüfung und härte," *Zeitschrift des Vereines Deutscher Ingenieure* 52 (1908): 645–654.

64. International Organisation for Standardisation, "BS EN ISO 18265:2013: Metallic Materials. Conversion of Hardness Values," (2013).

65. C. M. Sonsino, "Effect of Residual Stresses on the Fatigue Behaviour of Welded Joints Depending on Loading Conditions and Weld Geometry," *International Journal of Fatigue* 31 (2009): 88–101.

66. I. Weich, "Ermüdungsverhalten mechanisch nachbehandelter Schweißverbindungen in Abhängigkeit des Randschichtzustands. Institut für Bauwerkserhaltung und Tragwerk, TU Braunschweig," (2009).

67. T. Ummenhofer and P. Weidner, "Improvement Factors for the Design of Welded Joints Subjected to High Frequency Mechanical Impact Treatment," *Steel Construction* 6 (2013): 191–199.

68. L. Tong, L. Niu, Z. Ren, and X. L. Zhao, "Experimental Investigation on Fatigue Behavior of Butt-Welded High-Strength Steel Plates," *Thin-Walled Structures* 165 (2021): 107956.

69. International Organisation for Standardisation, "BS EN ISO 10360-8:2013: Geometrical Product Specifications (GPS). Acceptance and Reverification Tests for Coordinate Measuring Systems (CMS). CMMs With Optical Distance Sensors," (2013).

70. Creaform Inc, "VXelements," (2021).

71. ZEISS Group, "GOM Inspect Software Evaluation Software for 3D Point Clouds," (2021).

72. International Association of Classification Societies, "Recommendation No.47 Shipbuilding and Repair Quality Standard," (2013).

73. British Standards Institution, "BS EN ISO 5817:2023: Welding. Fusion-Welded Joints in Steel, Nickel, Titanium and Their Alloys (Beam Welding Excluded). Quality Levels for Imperfections," (2023).

74. DNV GL, "DNVGL-CG-0129: Fatigue Assessment of Ship Structures," no October, (2015): 1–129.

75. DNV G, "Fatigue Design of Offshore Steel Structures. Recommended Practice DNVGL-RP-C203," (2016): 20: 2016.

76. N. Ma, D. Deng, N. Osawa, S. Rashed, H. Murakawa, and Y. Ueda, *Welding Deformation and Residual Stress Prevention* (Butterworth-Heinemann, 2022).

77. L.-E. Lindgren, "Finite Element Modeling and Simulation of Welding Part 1: Increased Complexity," *Journal of Thermal Stresses* 24 (2001): 141–192.

78. E. R. Denlinger, J. C. Heigel, and P. Michaleris, "Residual Stress and Distortion Modeling of Electron Beam Direct Manufacturing Ti-6Al-4V," *Proceedings of the Institution of Mechanical Engineers - Part B: Journal of Engineering Manufacture* 229 (2015): 1803–1813.

79. M. B. Prime, "Cross-Sectional Mapping of Residual Stresses by Measuring the Surface Contour After a Cut," *Journal of Engineering Materials and Technology* 123 (2001): 162–168.

80. International Organisation for Standardisation, "BS EN ISO 10360-2:2009: Geometrical Product Specifications (GPS). Acceptance and Reverification Tests for Coordinate Measuring Machines (CMM). CMMs Used for Measuring Linear Dimensions," (2010).

81. D. Boruah, N. Dewagtere, B. Ahmad, et al., "Digital Image Correlation for Measuring Full-Field Residual Stresses in Wire and Arc Additive Manufactured Components," *Materials* 16 (2023): 1702.

82. Q. Zhang and J. Wang, "Accurate Evaluation on Residual Stress Considering Solid-State Phase Transformation and Initial Stress in Thick Weld," *Proceedings of the Institution of Mechanical Engineers, Part C: Journal of Mechanical Engineering Science* 236 (2022): 9661–9676.

83. S. M. O. Tavares and P. M. S. T. de Castro, "Residual Stress," in *Damage Tolerance of Metallic Aircraft Structures: Materials and Numerical Modelling*, eds. S. M. O. Tavares and P. M. S. T. de Castro (Springer International Publishing, 2019): 67–90.

84. D. Kollár, I. Völgyi, and A. L. Joó, "Development of Residual Stress Model of Orthotropic Steel Decks Using Measurements," in *Structure*, vol. 58 (Elsevier, 2023).

85. A. Chiocca, F. Frendo, F. Aiello, and L. Bertini, "Influence of Residual Stresses on the Fatigue Life of Welded Joints. Numerical Simulation and Experimental Tests," *International Journal of Fatigue* 162 (2022): 106901.

86. International Institute of Welding, "Recommendations for Fatigue Design of Welded Joints and Components," Paris, (2008).

87. M. M. Pedersen, "Thickness Effect in Fatigue of Welded Butt Joints: A Review of Experimental Works," *International Journal of Steel Structures* 19 (2019): 1930–1938.

88. V. Okenyi, S. Afazov, N. Mansfield, et al., "Corrosion Surface Morphology-Based Methodology for Fatigue Assessment of Offshore Welded Structures," *Fatigue and Fracture of Engineering Materials and Structures* 46 (2023): 4663–4677.

89. W. Zhao and W.-T. Hsu, "Re-Evaluation of Fatigue Thickness Effect Based on Fatigue Test Database," *Journal of Marine Science and Engineering* 8 (2020): 895.

90. S. J. Maddox, *Fatigue Strength of Welded Structures* (Woodhead Publishing, 1991).

91. S. J. Maddox, "Fitness-For-Purpose Assessment of Misalignment in Transverse Butt Welds Subject to Fatigue Loading," TWI, (1985).